EARTH SURFACE PROCESSES AND LANDFORMS
*Earth Surf. Process. Landforms* **42**, 2505–2522 (2017)

Published online 7 August 2017 in Wiley Online Library
(wileyonlinelibrary.com) DOI: 10.1002/esp.4194

# Reconstructing extreme post-wildfire floods: a comparison of convective and mesoscale events

**Daniel J. Brogan,[1]* Peter A. Nelson[1] and Lee H. MacDonald[2]**
[1] Department of Civil and Environmental Engineering, Colorado State University, Fort Collins, CO 80523-1372, USA
[2] Department of Ecosystem Science and Sustainability, Colorado State University, Fort Collins, CO 80523-1476, USA

Received 7 July 2015; Revised 9 June 2017; Accepted 19 June 2017

*Correspondence to: Daniel Brogan, Department of Civil and Environmental Engineering, Colorado State University, Fort Collins, CO 80523-1372, USA. E-mail: daniel.brogan@colostate.edu

ESPL
Earth Surface Processes and Landforms

ABSTRACT: In much of western United States destructive floods after wildfire are frequently caused by localized, short-duration convective thunderstorms; however, little is known about post-fire flooding from longer-duration, low-intensity mesoscale storms. In this study we estimate and compare peak flows from convective and mesoscale floods following the 2012 High Park Fire in the ungaged 15.5 $km^2$ Skin Gulch basin in the northcentral Colorado Front Range. The convective storm on 6 July 2012 came just days after the wildfire was contained. Radar data indicated that the total rainfall was 20–47 mm, and the maximum rainfall intensities (upwards of 50 mm $h^{-1}$) were concentrated over portions of the watershed that burned at high severity. The mesoscale storm on 9–15 September 2013 produced 220–240 mm of rain but had maximum 15-min intensities of only 25–32 mm $h^{-1}$.

Peak flows for each flood were estimated using three independent techniques. Our best estimate using a 2D hydraulic model was 28 $m^3 s^{-1} km^{-2}$ for the flood following the convective storm, placing it among the largest rainfall-runoff floods per unit area in the United States. In contrast, the flood associated with the mesoscale flood was only 6 $m^3 s^{-1} km^{-2}$, but the long-duration flood caused extensive channel incision and widening, indicating that this storm was much more geomorphically effective. The peak flow estimates for the 2013 flood had a higher relative uncertainty and this stemmed from whether we used pre- or post-flood channel topography. The results document the extent to which a high and moderate severity forest fire can greatly increase peak flows and alter channel morphology, illustrate how indirect peak flow estimates have larger errors than is generally assumed, and indicate that the magnitude of post-fire floods and geomorphic change can be affected by the timing, magnitude, duration, and sequence of rainstorms. Copyright © 2017 John Wiley & Sons, Ltd.

KEYWORDS: extreme flooding; geomorphology; wildfire; hydraulics; hydrology

## Introduction

High and moderate severity wildfires consume much of the overlying vegetation and litter, and high severity fires alter surface soils (Parsons *et al.*, 2010). The loss of surface cover and soil organic matter, reduction in surface roughness, and increased soil water repellency cause a dramatic decline in the soil infiltration rate (Shakesby and Doerr, 2006; Onda *et al.*, 2008; Larsen *et al.*, 2009; Ebel *et al.*, 2012) with a corresponding potential for large increases in infiltration-excess overland flow and surface erosion (Moody and Martin, 2001b). These large increases in hillslope-scale runoff and erosion can lead to extensive rilling and gullying, expansion of the drainage network in the steeper headwater areas (Moody and Martin, 2001a; Wohl, 2013) and dramatic downstream increases in flooding, erosion, and sedimentation (Doehring, 1968; Anderson, 1976; Moody and Martin, 2009). Burning of the riparian vegetation can further exacerbate these effects by reducing bank stability and exposing the riparian zone to channel scour (Eaton and Giles, 2008). The legacy effect of these fire-induced geomorphic changes can persist for tens to thousands of years (Meyer *et al.*, 1992, 1995; Elliott and Parker, 2001; Moody and Martin, 2001a; Legleiter *et al.*, 2003).

The effects of high and moderate severity wildfires on runoff and erosion are of increasing concern due to the growing population in the wildland–urban interface, and the increasing area and severity of wildfires due to climate change, earlier snowmelt, and historic wildfire suppression (Westerling *et al.*, 2006; Liu *et al.*, 2013; Rocca *et al.*, 2014). Given the current and projected increases in the number, extent, and severity of forest fires in the western USA and elsewhere (Flannigan *et al.*, 2009; Littell *et al.*, 2009), there is an urgent need to quantify the effects of wildfires on peak flows at the watershed scale.

For much of the western USA, the largest and most destructive floods after wildfires are caused by localized, short-duration convective thunderstorms (Morris and Moses, 1987; Meyer *et al.*, 1995; Cannon *et al.*, 2001; Moody and Martin, 2001a). The localized and usually remote nature of these storms means that the resulting peak flows are almost never measured on gaged watersheds, with very few exceptions (Canfield *et al.*, 2005; Kunze and Stednick, 2006). Rainfall-runoff generated floods from high-intensity, short duration

convective storms have been widely recognized, while post-fire floods from low-intensity, long duration mesoscale storms are very uncommon and remain largely unstudied.

Following a wildfire disturbance in Colorado in 2012 we had the opportunity to investigate two post-wildfire floods generated by different types of rainstorms. The first flood on 6 July 2012, just a few days after the fire was fully contained, was the response to a localized convective storm, and is referred to as the 'convective flood' throughout this paper. The second flood was in September 2013, 15 months after the fire, and this was caused by a lower-intensity, but unusually large and long-duration storm. This second storm is referred to as the 'mesoscale flood' throughout this paper.

The juxtaposition of these two different rainstorms and resulting large floods allowed us to investigate the relationships between rainfall amount and intensity, flood response, and geomorphic changes after wildfire. Here we seek answers to two key questions: (1) how do the peak flows and geomorphic changes from the unusual mesoscale storm compare with the peak flows and post-flood geomorphology from the convective storm? (2) What is the importance of local rainfall intensity, bare soils, and sequence of events on the magnitude of the peak flows from each of these two storms? In our efforts to answer these two questions, we had to answer a third and more basic set of questions, namely: (3) how precisely can we estimate the peak flows from each storm? And can our confidence in the estimated peak flows be improved by using and comparing different estimation techniques?

In this study we used the slope-area method, critical flow method, and a 2D hydraulic model to estimate the peak flows from the convective and mesoscale flood. The occurrence of the mesoscale flood meant that we could directly compare the differences in the estimated peak flows using pre- and post-flood topography for each of the three estimation techniques. The intercomparisons of the estimated peak flows among techniques, the different cross-sections, and the pre- and post-flood topography provides insights into the inherent uncertainties and validity of each estimation technique. The exceptionally high magnitude of our estimated peak flows then led us to a fourth question, which was: (4) how do the unit area magnitudes of these peak flows compare with other large rainfall-runoff generated floods in the United States? The answers to these four questions are useful for assessing the potential magnitude and effects of post-fire floods resulting from two very different types of rainstorms, and have much broader implications for the techniques and uncertainties in quantifying peak flows after major floods.

## Site description and background

The 2012 High Park Fire wildfire (HPF) was ignited by a lightning strike on 9 June 2012 in the northcentral Colorado Front Range. It burned 353 $km^2$ and nearly 260 homes by the time it was 100% contained on 1 July (HPF BAER Report, 2012). Our study focused on the main branch in the Skin Gulch (SG) basin (15.5 $km^2$) that is located nearly in the middle of the HPF burn area (Figure 1) with elevations ranging from 1890 to 2580 m, and a main channel width of ~1 m at base flow. Geology of the basin is primarily Precambrian metasedimentary and metaigneous schists, gneisses, and plutonic igneous rocks (Abbott, 1970), and the soils are typically sandy loams with 10–60% rock content by volume at the surface and 35–80% in the subsurface (HPF BAER Report, 2012). Annual precipitation averages about 450–550 mm (PRISM Climate Group,

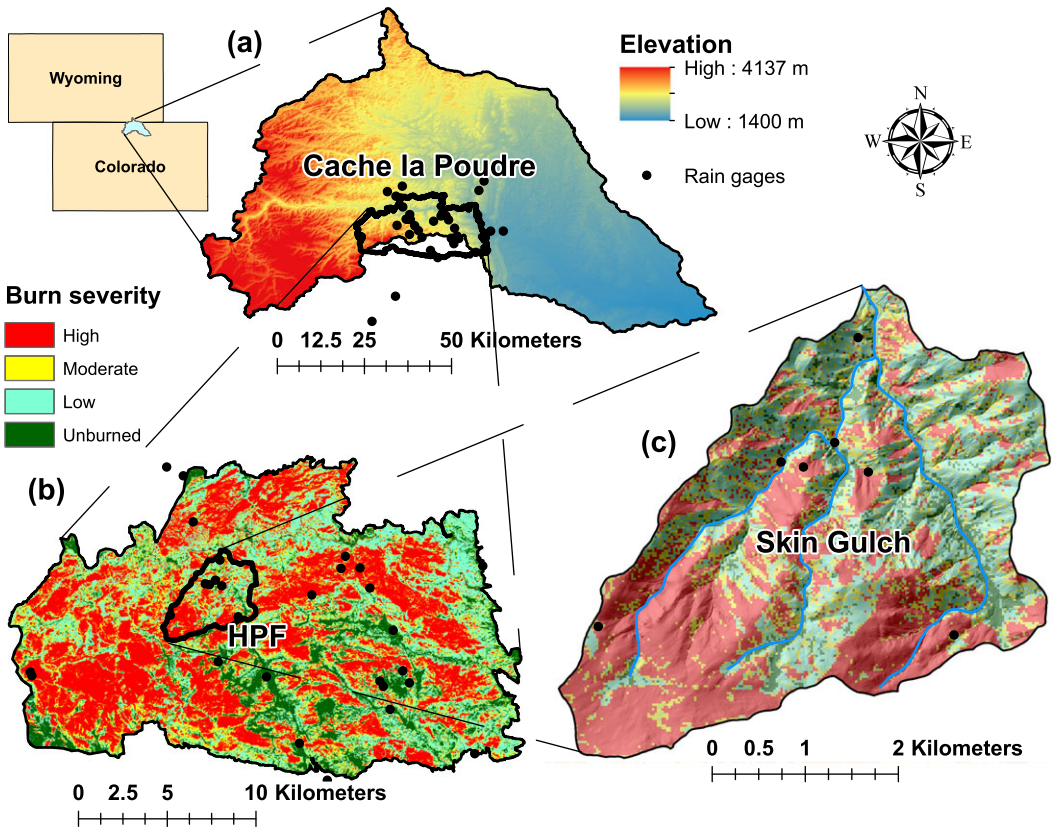


**Figure 1.** Location and elevation of the (a) Cache la Poudre basin in the Colorado Front Range of the western USA, and burn severity in the (b) High Park Fire and (c) Skin Gulch, respectively. Black dots show the location of rain gages used to characterize the September 2013 mesoscale storm. [Colour figure can be viewed at wileyonlinelibrary.com]

Oregon State University, http://prism.oregonstate.edu, map created 19 Feb 2015), with most of the precipitation from November to May falling as snow. Summer precipitation comes mostly from convective storms. Vegetation in SG prior to the HPF was 81% evergreen forest (primarily ponderosa pine), 15% shrub/scrub, and ~4% deciduous forest, grassland/herbaceous and woody wetland (data derived from the 2011 National Land Cover Database; Jin *et al.*, 2013). RapidEye imagery and a multistage decision tree indicated that approximately 44% of the drainage area burned at high severity, 21% at moderate severity, 35% at low severity, and just 6% unburned (Figure 1(c)). Within Skin Gulch the majority of the area burned at high severity was in the headwaters and west-central part of the watershed.

The convective flood on 6 July 2012 was centered over one main tributary that had burned at high severity. This flood mobilized large amounts of sediment, and deposited cobbles, large boulders, and woody debris in the mainstem channel and valley bottom (Figure 2). At that time we had no on-site rainfall data or detailed topographic data, although we had surveyed one cross-section at the base of the watershed prior to the flood. The ash and sediment delivered from this and subsequent floods to the Cache la Poudre (CLP) River affected the primary water supply for several hundred thousand people (Writer *et al.*, 2014).

The mesoscale flood in September 2013 affected the entire central and northern Colorado Front Range, resulting in widespread flooding that washed out numerous major highways (Gochis *et al.*, 2014; Yochum, 2015) and triggered over 1100 landslides and debris flows (Anderson *et al.*, 2015). This flood caused extensive geomorphic change in SG (Figure 3), and for this flood we had rainfall data from seven tipping bucket rain gages and detailed pre- and post-flood topographic data (Kampf *et al.*, 2016).


**Figure 2.** Pictures taken after the convective flood (6 July 2012) indicate the extreme magnitude of this flood. (a) Imbricated boulders above the channel bed looking at the left bank between cross-section (XS) 8 and XS9; (b) extensive deposits of boulders and cobbles on the floodplain looking upstream just downstream from the confluence of Tributary 3; and (c) large pileup of woody debris looking upstream from XS6. See Figure 4 for XS and tributary locations. [Colour figure can be viewed at wileyonlinelibrary.com]

## Methods

### Field observations

Ten channel cross-sections for repeat surveys were established over the course of several months following the HPF. There were only six days between containment of the HPF and the first rainstorm and associated flood on 6 July, so the only channel data from SG was a single cross-section (XS) that was established near the outlet of SG on 4 July (XS1 in Figure 4). The sediment deposits and high water marks (HWM) from the 6 July 2012 flood extended well beyond the original surveyed cross-section. On 22 July 2012 a longer cross-section was re-established at the same location, and on the same day XS2 was established farther upstream. In early fall 2012 seven additional cross-sections were established on straight reaches along the main branch of SG, and these were selected to represent erosional, depositional, and transport reaches. One additional cross-section was established on Tributary 3 (Figure 4), which appeared to be unaffected by the flood. Above XS1 drainage areas along the main channel ranged from 9.04 $km^2$ at XS2 to 4.63 $km^2$ at XS10 (Table I). Longitudinal profiles were established at each cross-section.

We also measured the intermediate axis of 60 of the larger imbricated particles deposited by the convective flood between XS6 and XS9. Frequent pictures and field visits showed that subsequent storms in summer 2012 caused minimal channel change, making us confident that the cross-section surveys accurately captured conditions after the convective flood.

The elevations of HWMs were measured for the convective and mesoscale floods throughout the basin, but not at every cross-section. These were identified after the convective storm by very distinct lines of deposited ash and fine debris, and after the mesoscale storm primarily by matted-down vegetation. All of the HWMs from the mesoscale flood were lower in elevation than the HWMs from the convective flood. For the convective flood two HWMs were noted near XS2 on 22 July 2012; subsequent field visits identified 53 HWMs along the main branch of SG (Figure 4). These HWMs were readily identified because no floods within the first year after burning came close to the magnitude of the 6 July 2012 flood. Forty-two HWMs were surveyed shortly after the mesoscale flood (Figure 4). In our analyses, we estimate an uncertainty in the elevation of the HWMs of 0.10 m, which reflects potential undulations in the free surface at peak discharge, and uncertainties of this


**Figure 3.** Photos looking downstream between cross-section (XS) 9 and XS10 (a) prior to and (b) after the mesoscale flood (September 2013) showing the large increase in the size of the channel. The same boulder is circled in red in both pictures. See Figure 4 for XS and tributary locations. [Colour figure can be viewed at wileyonlinelibrary.com]

magnitude have been used for indirect discharge analyses of the 2013 flood at other locations along the Colorado Front Range (Moody, 2016). Stage data were collected near XS1 during the mesoscale flood by an ultrasonic water level sensor, but these could not be used to calculate discharge because the bed aggraded by more than 2 m during this flood (Kampf *et al.*, 2016). Maximum inundated area and mean flow depth were calculated for each cross-section that had a nearby HWM by projecting a horizontal water surface elevation across the channel from the measured HWM. Absolute changes in cross-sectional area due to the mesoscale flood were summarized in Kampf *et al.* (2016).

The 2012 surveys were conducted using either an autolevel and stadia rod, or a Leica TCR407 total station. The 2013 surveys were conducted with a Topcon GR-5 Real-Time Kinematic Global Navigation Satellite Systems (RTK-GNSS). The total station data were rotated and adjusted for elevation using benchmarks to match the real-world RTK-GNSS coordinates. Average estimated horizontal and vertical root mean square error (HRMS and VRMS) among the methods was 6 mm and 10 mm, respectively.

## Lidar data and model domains

Three airborne lidar datasets covering the SG watershed were used as topographic input for the 2D modeling of each flood. The first two sets of data were collected in October 2012 and July 2013 by the National Ecological Observatory Network (NEON) Airborne Observation Platform. The third airborne lidar dataset was collected by the USGS 1 month after the mesoscale flood. The primary product from each dataset was a 1 m bare-earth digital elevation model (DEM). The DEMs developed from the two NEON datasets required a mean bias correction (i.e. elevation adjustment) to fit our surveyed cross-sections as there was a lack of vertical ground control and possible transformation errors between the NAD83 and WGS84 ellipsoids. After correction the mean absolute error (MAE) between our RTK-GNSS survey data and the lidar surfaces was reduced to 0.13 m for the 2012 NEON DEM ($n = 2575$) and 0.19 m for the 2013 NEON DEM ($n = 2437$). The MAE for the 2013 USGS lidar was 0.24 m ($n = 3060$).

Field observations after the convective storm indicated that the high peak flows and associated channel geomorphic changes were confined to the main stem of SG given the general lack of channel change, HWMs or deposition in the tributaries (Figure 4). It was therefore surmised that the tributaries contributed negligible flow during this flood. To take advantage of as many HWMs as possible, the areal domain for the 2D modeling of the convective flood began upstream of XS2 and extended to just upstream of XS10 (Figure 4). The contributing area at the upstream end of this model domain was 4.6 $km^2$, and the HWMs throughout this reach were longitudinally widespread.

In contrast, field observations for the mesoscale flood indicated substantial flows and geomorphic changes throughout the watershed, so it was not possible to use the same domain as for the convective flood. The model domain for the mesoscale flood was therefore focused on the lower portion of the main channel from just below XS2 upstream to the confluence of the main channel with Tributary 3 (Figure 4). Although this domain covers a different spatial area than the model domain for the convective flood, they do overlap, and because our models were run under steady-state conditions (discussed below) the different spatial domains should not affect peak flow comparisons. For the mesoscale flood we used the 11 HWMs between XS2 and XS4, which were primarily on the inside of a bend or along one side of straight reaches. The contributing area upstream of XS4 is 8.7 $km^2$.

## Precipitation

The convective storm on 6 July 2012 occurred prior to the installation of any tipping-bucket rain gages, so radar data were used to estimate precipitation from that storm. Amount and intensity of rainfall were determined from 15 min radar data (Hydro-NEXRAD, Krajewski *et al.*, 2011) collected by the National Weather Service (NWS) Doppler radar in Cheyenne, Wyoming, which is approximately 70 km northeast of the study basin. The storm had two main rainfall bursts that were 7 h apart with each burst lasting less than 1.5 h. The radar data were gridded in ~1 $km^2$ bins and bias-corrected with daily rainfall data from 16 nearby Community Collaborative Rain, Hail and Snow Network (CoCoRaHS) rain gages (Cifelli *et al.*, 2005). Because the CoCoRaHS data are daily totals collected at 0700 local time, the radar data were summed to obtain daily totals for the 24 h period ending at 0700. A daily mean field bias (MFB) correction was calculated as:

$$B_i = \frac{\sum G_{ij}}{\sum R_{ij}} \quad (1)$$

where $B_i$ is the multiplicative bias for a particular day $i$, $G_{ij}$ is the daily rainfall for day $i$ and gage $j$, and $R_{ij}$ is the summed

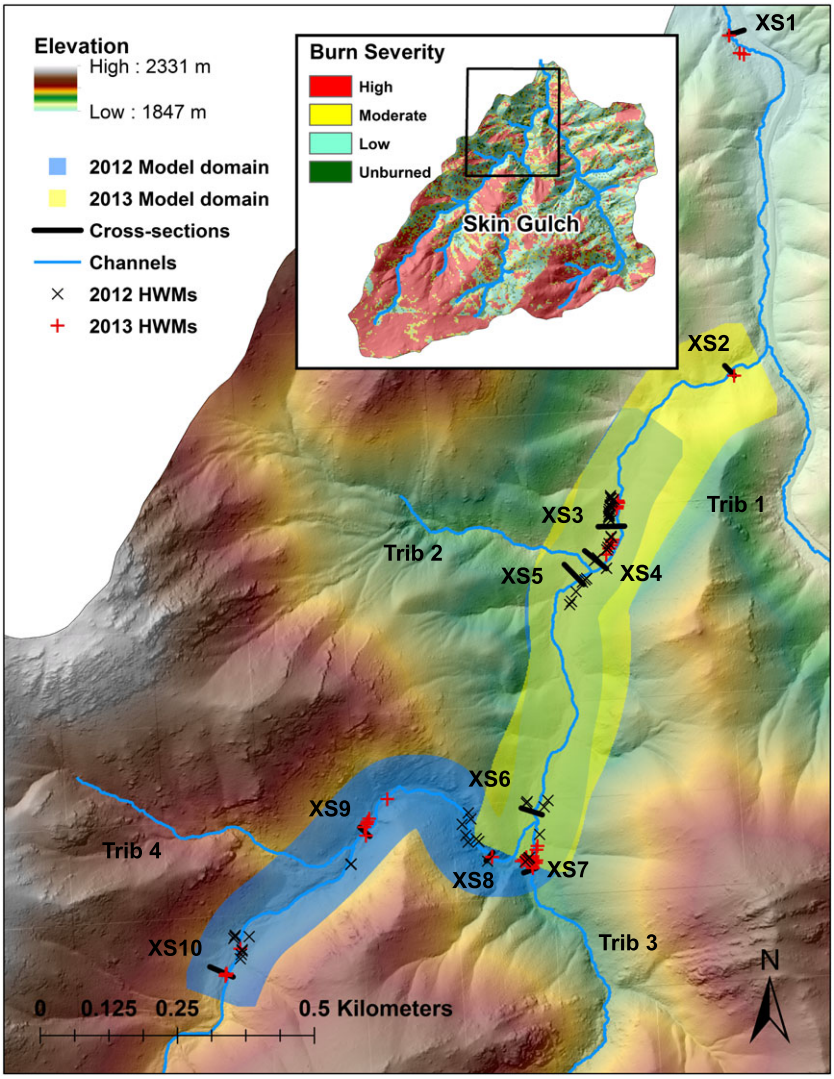


**Figure 4.** Shaded relief map of lower Skin Gulch showing major tributaries, cross-sections (XS), high water marks (HWMs), and hydraulic model boundaries. Inset shows burn severity for the entire SG watershed. [Colour figure can be viewed at wileyonlinelibrary.com]

**Table I.** Drainage areas for each cross-section along with the net cross-sectional erosion and deposition due to the mesoscale flood. Net erosion and deposition for the convective flood could not be calculated because pre-flood surveys do not exist

| Cross-section | Drainage area ($km^2$) | Erosion ($m^2$) | Deposition ($m^2$) | Net change ($m^2$) |
|---|---|---|---|---|
| **XS2** | 9.04 | −2.4 | 0.6 | −1.8 |
| **XS3** | 8.79 | −2.8 | 2.2 | −0.6 |
| **XS4** | 8.77 | −21.9 | 2.1 | −19.8 |
| **XS5** | 8.33 | −14.7 | 3.4 | −11.3 |
| **XS7** | 2.80 | −1.6 | 0.0 | −1.6 |
| **XS8** | 5.21 | −7.6 | 0.2 | −7.4 |
| **XS9** | 5.12 | −4.6 | 0.1 | −4.5 |
| **XS10** | 4.63 | −4.7 | 0.3 | −4.4 |

24 h rainfall for day *i* and the radar pixel containing gage *j* (Wright *et al.*, 2013). The calculated bias was 0.95, and this value was used to correct all of the 15 min radar rainfall estimates.

Seven tipping-bucket rain gages installed after July 2012 in SG recorded the mesoscale storm. The radar data accurately estimated the total precipitation for this storm but did not accurately reproduce the 15 min rainfall intensities, possibly due to terrain beam blockage (Zrnić and Ryzhkov, 1996). Thus the rainfall over SG was estimated by natural neighbor interpolation of the rain gage data. To match other studies (i.e. Lukas *et al.*, 2013) we defined the duration of the mesoscale storm from 0700 mountain daylight time (MDT) on 9 September to 0700 MDT on 16 September 2013. Recurrence intervals for the convective and mesoscale storms were determined from NOAA atlas precipitation-frequency data (Perica *et al.*, 2013).

## Peak flow estimation techniques

Three different techniques were used to estimate peak flows from each flood: (1) the slope-area method; (2) the critical flow method; and (3) two-dimensional hydraulic modeling with Nays2D. Peak flow estimates for the convective flood were necessarily based on the topographic data collected after the flood, while peak flows for the mesoscale flood were estimated using both the pre- and post-flood topography. Uncertainty in each method was computed using a Gaussian error propagation approach.

For the slope-area method we used Manning's equation:

$$Q = \frac{AR^{2/3}S^{1/2}}{n} \tag{2}$$

where $Q$ is the discharge ($m^3 s^{-1}$), $V$ is the mean cross-section velocity ($m s^{-1}$), $A$ is the cross-sectional area of the flow ($m^2$), $R$ is the hydraulic radius (m), $S$ is the mean water surface slope (m/m), and $n$ is Manning's roughness coefficient ($s/m^{1/3}$). Slope was approximated from the local bed slopes over a 50 m reach since the HWMs were spaced too intermittently to be used to calculate water surface slope. Equation (2) was only used at cross-sections with nearby measured HWMs, so peak flows were estimated at five cross-sections for the convective flood (2, 3, 4, 5 and 8) and four cross-sections for the mesoscale flood (2, 7, 9 and 10). Note that XS7 is on a tributary to the main stem (Figure 4), and our cross-sections were established to document channel change rather than estimate peak flows. Hence our cross-sections were not replicated as suggested by Dalrymple and Benson (1967).

For each cross-section we made eight estimates of Manning's $n$ using standard empirical equations (Limerinos, 1970; Hey, 1979; Jarrett, 1984; Dingman and Sharma, 1997; Ferguson, 2007), reference tables (Chow, 1959; Arcement and Schneider, 1989), and photographic guides (Barnes, 1967). Peak flow using the slope-area method was then calculated using the mean of these $n$ values. Uncertainties in the peak flow estimates were computed using Gaussian error propagation, in which the uncertainty in the horizontal and vertical measurement of each survey point was taken to be the horizontal and vertical root mean square error (HRMS and VRMS) from the RTK-GNSS; vertical uncertainty in the HWMs was assumed to be 0.10 m as noted above; uncertainty in the slope was taken to be the standard error from the linear regression used to compute the slope; and uncertainty in Manning's $n$ was the standard deviation from the suite of empirical estimates at each location.

The second method to estimate peak flows was the critical flow method, and this calculates discharge by assuming the Froude number is equal to one. Based on this assumption and conservation of mass, discharge is calculated by:

$$Q = A\sqrt{g\overline{h}} \tag{3}$$

where $g$ is gravitational acceleration ($9.81 m/s^2$) and $\overline{h}$ is the average flow depth (m). The same cross-sections and HWMs were used for the critical flow method as the slope-area method. Uncertainty in the peak flow estimates was again computed using Gaussian error propagation where uncertainty in the horizontal and vertical position of each survey point and the estimated uncertainty in the HWM elevations were used. Previous literature has shown that the Froude number varies considerably during floods (Costa, 1987; Lumbroso and Gaume, 2012), so we also assign and propagate a 20% uncertainty to the assumed Froude value of one.

The third method used to estimate peak flows was the Nays2D model (Asahi *et al.*, 2013), where a series of steady-state constant discharges were simulated in order to find the peak discharge that best matched the surveyed HWMs. Nays2D is an open-source model distributed with the iRIC interface (International River Interface Cooperative, http://i-ric.org; Nelson *et al.*, 2015). It solves the 2D depth-averaged equations of fluid continuity and momentum to determine water surface elevations and depth-averaged velocities. These equations are solved in a general curvilinear coordinate system, enabling computational meshes of any shape. For the convective and mesoscale simulations we constructed a computational mesh of curvilinear quadrilateral cells with a spacing of approximately 2 m in the downstream direction and 1 m in the lateral direction.

To estimate the convective flood the grid cells were assigned elevations by interpolating the 2012 NEON lidar data. Similarly for the mesoscale flood we used the 2013 NEON lidar data and the 2013 USGS lidar data to develop meshes for pre- and post-flood topography, respectively. Upstream and downstream boundary conditions were set to uniform flow. Each simulation was run with a time step of 0.01 s for a total of 1000 s, at which point the flows were at steady-state. The cubic-interpolated pseudoparticle method was used for finite differential calculation of the advection terms. The zero-equation model was used for eddy viscosity parameterization:

$$v_t = C\frac{k}{6}u_* h \tag{4}$$

where $v_t$ is the eddy viscosity coefficient, $k$ is the von Karman coefficient (0.4), $u_*$ is the shear velocity ($m s^{-1}$), and $h$ is depth (m), and $C$ is a user-defined parameter for which we used the default setting ($C = 1$).

The primary outputs from each 2D simulation were the local depth ($h$) and the 2D depth-averaged velocity vectors ($u$, $v$). Boundary shear stress ($\tau_x$, $\tau_y$) in Nays2D is calculated with a drag coefficient closure:

$$(\tau_x, \tau_y) = \rho C_d \sqrt{u^2 + v^2}(u, v) \tag{5}$$

where $\rho$ is the density of the fluid ($kg/m^3$), and $C_d$ is the drag coefficient as calculated by:

$$C_d = \frac{gn^2}{h^{1/3}} \tag{6}$$

This parameterization, which is also used in the momentum equation, allows roughness to decrease with increasing flow depth despite using a spatially uniform $n$.

We used Nays2D to estimate the peak discharge for each flood by applying the mean estimate of all empirical Manning's $n$ estimates, and imposing a constant discharge. We ran numerous simulations where discharge was varied from 5 to 250 $m^3 s^{-1}$ in 5 to 10 $m^3 s^{-1}$ increments. For each simulation the mean absolute error (MAE) was calculated from the differences between the water surface elevation of the inundated grid cell closest to the surveyed elevation of each measured HWM (53 for the convective flood and 11 for the mesoscale flood). Our best estimate of the peak flow was the discharge with the minimum MAE.

We characterized the uncertainty of the 2D–model-estimated peak discharges by separately accounting for uncertainty in roughness and uncertainty in HWM elevations. To account for uncertainty in Manning's $n$, we repeated the series of simulations twice with roughness values equal to the mean value minus and plus the standard deviation of the distribution of empirical estimates, respectively. The range of discharges that minimized the MAE for these two $n$ values were considered to represent the uncertainty in peak flow due to roughness parameterization.

To account for uncertainty in HWM elevation in the 2D modeling, we used the series of simulations where the roughness was the mean Manning's $n$ estimate, and we shifted the HWM elevations vertically up or down by the uncertainty in the relative HWM elevation (0.10 m) plus the uncertainty in the lidar (0.13 to 0.24 m, as discussed above). The MAEs between these adjusted HWM elevations and model outputs were computed, and the discharges that minimized the MAE were taken to represent the uncertainty in peak flow due to HWM elevation uncertainty.

In order to test for the effects of hyperconcentrated flows we varied the fluid density from 1000 to 2000 $kg/m^3$ and $C$ in the eddy viscosity term from 0.1 to 10. Since these variations did not change the discharge associated with the minimum MAE and had a negligible effect on the absolute MAE, they are not further reported.

Using the best estimates of peak flows from Nays2D we estimate reach average peak unit stream power ($\omega$) as:

$$\omega = \frac{\gamma Q S}{w} \quad (7)$$

where $\gamma$ is the specific weight of the fluid (N/m$^3$), $Q$ is the peak discharge, and $w$ is the mean channel width (m). Mean channel width and water surface slopes were estimated from the Nays2D model outputs. We also make a rough estimate of the total energy expenditure during each flood by integrating the time series of stream power, assuming it has a triangular shape with a duration estimated from the rainfall data and the peak estimated from Equation (7).

## Results

### Precipitation – Convective storm

Rainfall for the convective storm on 6 July 2012 was highly variable in space and lasted about 19.5 h. Total rainfall varied from 47 mm in the western portion of the watershed to only about 20 mm in the eastern portion of the watershed (Figure 5(a)). Peak 15-min rainfall intensities ($I_{15}$) ranged from about 10 to 50 mm h$^{-1}$, with the highest intensity in the southern portion of the watershed over an area that burned at high severity (Figure 5(b)). The rainfall came primarily in two short bursts, with the first burst being spatially more widespread with most 15 min intensities exceeding 27 mm h$^{-1}$ and peak 15 min intensities approaching 50 mm h$^{-1}$ (Figure 6(a)). Rainfall intensities dropped to only 10–15 mm h$^{-1}$ at the eastern boundary of the watershed (Figure 5(b)). The second burst was less widespread and less intense (Figure 6(a)), indicating that the flood was almost certainly due to the initial burst at around 1415 MDT. Recurrence intervals for these depths and maximum 15 min intensities are roughly 1–10 and less than 2 years, respectively (Perica *et al.*, 2013).

### Precipitation – mesoscale storm

In contrast to the convective thunderstorm, the mesoscale storm lasted roughly 7 days. This extreme storm was due to monsoonal moisture being directed to the central and northern Colorado Front Range (Lukas *et al.*, 2013; Gochis *et al.*, 2014). Rainfall amounts and intensities were quite uniform over the SG catchment, and total rainfall was about 220–235 mm or about five times the maximum total rainfall from the July storm (Figure 5(b)). Approximately 150–160 mm or 70% of the total rainfall fell in 24 h (Figure 6(b)), but the maximum 15 min intensities were only 25–31 mm h$^{-1}$ (Figures 5 (b) and 6(b)). The extreme nature of this storm is indicated by the estimated recurrence intervals of 200–500 years for

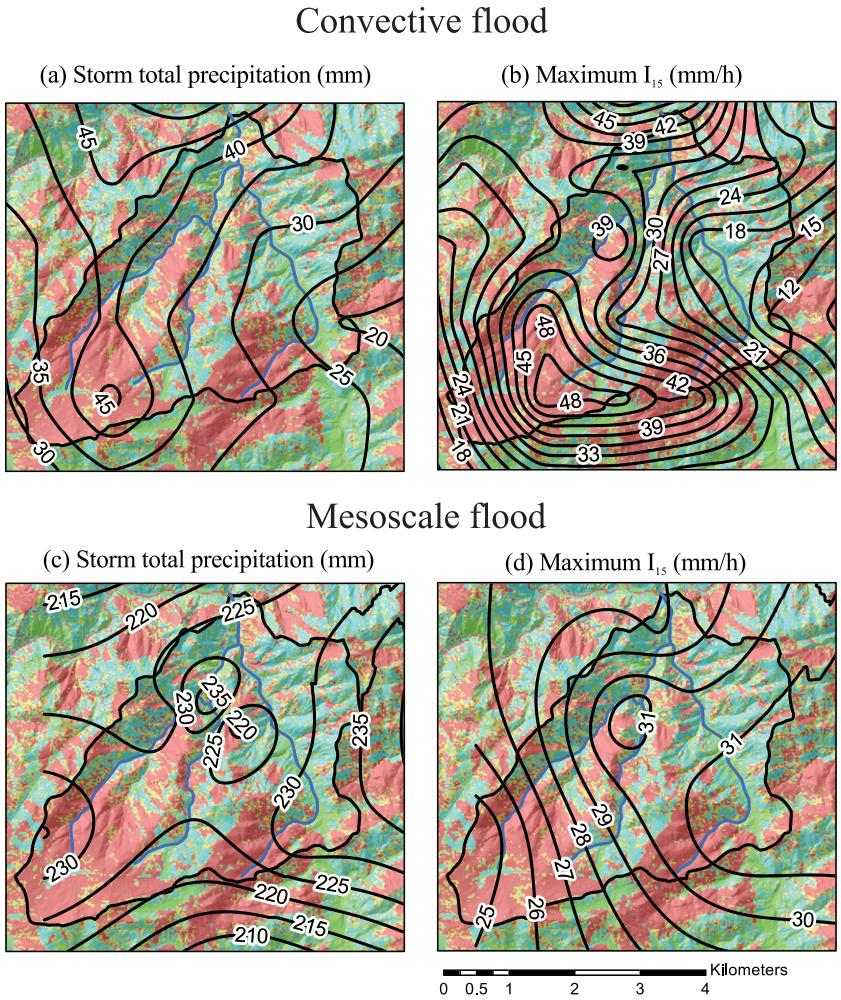


**Figure 5.** Isohyets of storm total precipitation (mm) and maximum 15-minute rainfall intensities (mm/h) over Skin Gulch for the convective storm on 6 July 2012 (a), (c) and mesoscale storm on 9–15 September 2013 (b), (d), respectively. The background of each figure is the burn severity map for the 2012 High Park Fire, where red is high severity, yellow is moderate severity, aquamarine is low severity, and green is unburned. [Colour figure can be viewed at wileyonlinelibrary.com]

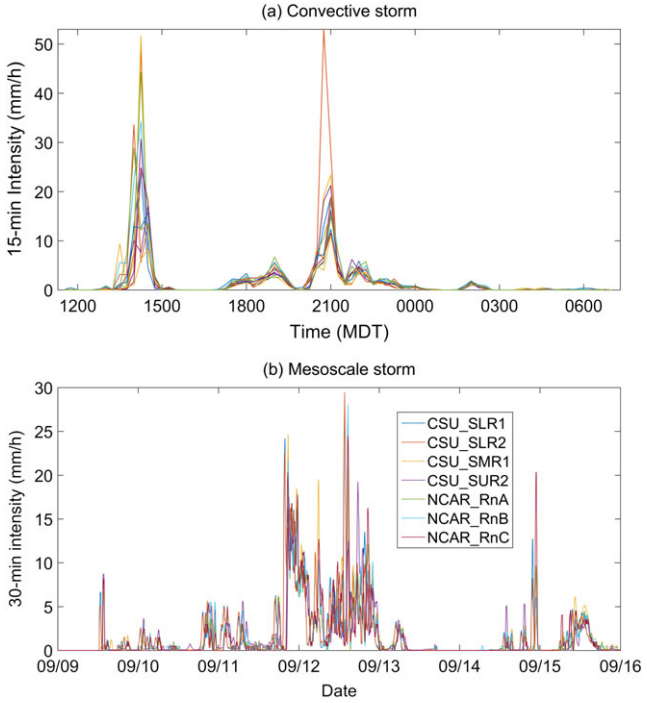


**Figure 6.** (a) 15-min rainfall intensities for the convective storm on 6 July 2012 computed from biascorrected Hydro-NEXRAD radar data; each line is the time series of a 1 km$^2$ radar bin within Skin Gulch. (b) 15-minute rainfall intensities from the mesoscale storm on 9–15 September 2013 for each recording rain gage in Skin Gulch with dates centered at 0000 MDT. Names in legend refer to rain gages installed and maintained by researchers from Colorado State University (CSU) and the National Center for Atmospheric Research (NCAR), respectively. [Colour figure can be viewed at wileyonlinelibrary.com]

the 1 day precipitation and roughly 500–1000 years for the 7 day precipitation (Perica *et al.*, 2013).

## Field observations of the convective and mesoscale floods

The convective flood led mainly to depositional geomorphic changes in the SG channel. The large magnitude of the peak flows coming from the upper mainstem of SG are shown by the boulder-sized clasts that were imbricated between XS8 and XS9, deep cobble and boulder deposits just below the confluence with Tributary 3 where the steep, bedrock-confined upper mainstem entered a roughly 40 m wide alluvial valley, and the ~2 m high deposits of woody debris against standing trees near XS6 (Figure 2). The mean diameter of the 60 imbricated boulders that we measured was just over 300 mm, and the largest had an intermediate axis of just over 1 m. Our observations of imbrication, a lack of levees, and fan and sheet deposits indicate that the convective flood was not a debris flow (Costa, 1988; Pierson and Costa, 1988; Pierson, 2005). The lack of HWMs in Tributary 3 or evidence of high flows in the numbered tributaries suggests that nearly all the water and sediment during the convective flood came from the western branch. The spatially varying geomorphic changes show how a highly localized, high-intensity rainfall can combine with high burn severity (Figure 5(a)) to produce a major flood in one portion of SG compared with the other portions that either had less rainfall or were not as severely burned.

The depositional nature of this flood was shown by the extensive deposits from XS8 all the way downstream to XS1. At XS1 there was a maximum vertical aggradation of 0.14 m and a 1.4 m$^2$ decrease in cross-sectional area, but there was much more deposition on the floodplain and terrace beyond the right-hand side of the cross-section.

In contrast to the depositional nature of the convective flood, the primary geomorphic changes from the long duration mesoscale flood were incision and widening (Table I; Figure 7 supplementary Figures S1–S10). Only XS1 experienced deposition, and the 2.3 m of aggradation was due to the backing up of a downstream culvert (Kampf *et al.*, 2016). The ultrasonic sensor at XS1 showed that high flows lasted for ~60 h beginning about 1845 MDT on 11 September 2013. At XS8 there was 1.7 m of incision and a corresponding decrease in the flood impacted channel width from 6 m to 4 m, while farther downstream at XS4 the flood expanded the active channel width from about 3 to 23 m with only 0.3 m of incision (Figure 7). Bank undercuts and bank failures were common along the lower mainstem, and the bank erosion helped trigger a shallow landslide at XS4.

## Estimated peak flows – Slope-area method

Cross-sectional flow areas and depths during the convective flood were greater than for the mesoscale flood (Table II), which accurately corresponds to the observed higher HWMs from the convective flood and erosional nature of the mesoscale flood. The mean Manning's *n* values among cross-sections increased from the convective flood to pre-mesoscale flood by ~0.005 and again by the same amount from the pre-mesoscale flood to post-mesoscale flood (Table II).

Peak flow estimates for the convective flood varied from 32 to 140 m$^3$ s$^{-1}$ (3.8 to 25 m$^3$ s$^{-1}$ km$^{-2}$), but we believe that the low value of 32 m$^3$ s$^{-1}$ is not representative as the HWM for this XS was on the inside of a bend within a stand of unburned trees (Table III; Figure 8). If this value is excluded the range is from 62 to 140 m$^3$ s$^{-1}$, with three of the four remaining cross-sections having values of 130–140 m$^3$ s$^{-1}$. There was a strong decrease in peak flows per unit area from 25 m$^3$ s$^{-1}$ km$^{-2}$ at XS8 to only 6.9 m$^3$ s$^{-1}$ km$^{-2}$ at XS2, and this is consistent with the locations of peak rainfall intensities and the expected decline in unit area peak flows with increasing drainage area (Smith et al., 2005a, b). The uncertainties in the estimated peak flow ranged from 13 to 78 m$^3$ s$^{-1}$ (1.6 to 13 m$^3$ s$^{-1}$ km$^{-2}$) depending on the cross-section, and these were proportional to the estimated peak flows in both absolute and unit area terms (Table III).

Using the slope-area method, estimated mesoscale flood peak flows were all smaller than the estimated peak flows for the convective flood (Table III). Excluding XS7 on Tributary 3, the estimated peak flows using pre-flood topography varied from 16 to 40 m$^3$ s$^{-1}$, while the peak flows per unit area varied from 1.8 to 8.7 m$^3$ s$^{-1}$ km$^{-2}$. Uncertainties were 9.7 to 21 m$^3$ s$^{-1}$ (1.1 to 4.6 m$^3$ s$^{-1}$ km$^{-2}$). Using the post-flood topography increased the estimated peak flows from 1.4 to 2.5 times, and this was due primarily to the greater channel cross-sectional area (Table II). Excluding XS7 on Tributary 3, the estimated peak flows using post-flood topography varied from 23 to 60 m$^3$ s$^{-1}$, while the peak flows per unit area varied from 2.5 to 13 m$^3$ s$^{-1}$ km$^{-2}$. Uncertainties were 11 to 28 m$^3$ s$^{-1}$ (1.2 to 6.0 m$^3$ s$^{-1}$ km$^{-2}$). Direct at-a-station comparisons between floods are difficult because only XS2 had HWMs and peak flow estimates for both floods. For this cross-section, the estimated peak flows for the mesoscale flood using pre- and post-flood topography were, respectively, 26% and 37% of the estimated values for the convective flood.

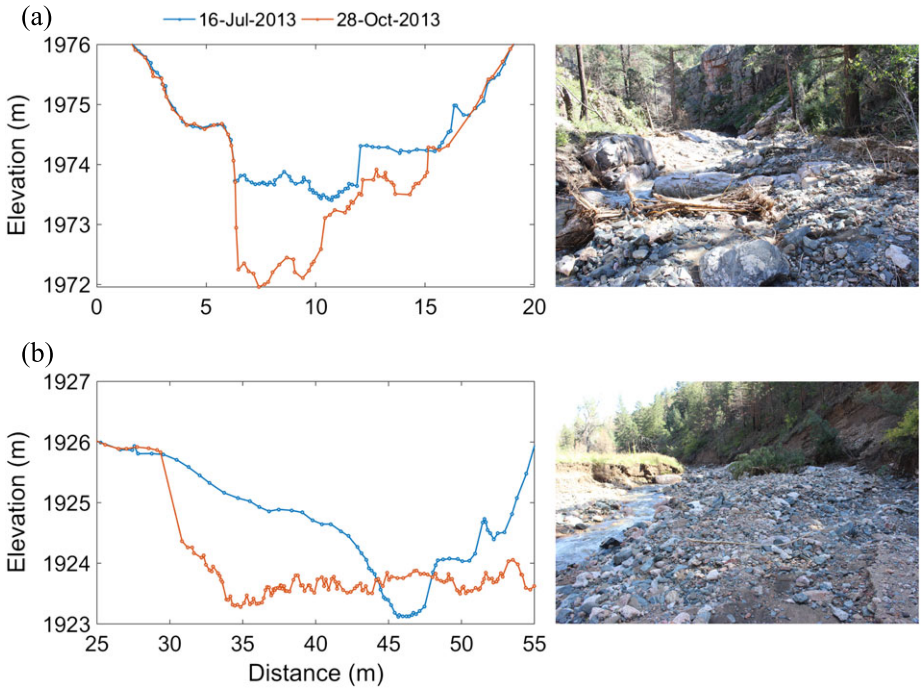


**Figure 7.** Plot of (a) XS8 and (b) XS4 prior to and after the mesoscale flood. The photos at each cross-section were taken on 24 September 2013 looking downstream. [Colour figure can be viewed at wileyonlinelibrary.com]

**Table II.** Inundated cross-sectional areas, mean flow depth, maximum flow depth and hydraulic radius as determined by the HWMs, local slopes, and statistics for Manning's *n* used for each cross-section and the Nays2D model. The rightmost Manning's *n* column presents the mean and standard deviation of all of the independent roughness estimates for the flood/topography, and were used in the Nays2D modeling of that flood. XS1 and XS6 are excluded because there were no nearby HWMs for either flood

| Flood | Topography | Cross-section | Area ($m^2$) | Mean flow depth (m) | Max flow depth (m) | Hydraulic radius (m) | Slope | Manning's *n* ($s/m^{1/3}$) | | | Manning's *n* ($s/m^{1/3}$) | |
|---|---|---|---|---|---|---|---|---|---|---|---|---|
| | | | | | | | | Mean | S.D. | Range | Mean | S.D. |
| Convective | Post-flood | XS2 | 17.7 | 0.8 | 1.3 | 0.9 | 0.034 | 0.05 | 0.03 | 0.03–0.09 | | |
| Convective | Post-flood | XS3 | 31.5 | 1.0 | 1.9 | 1.0 | 0.065 | 0.06 | 0.03 | 0.03–0.11 | | |
| Convective | Post-flood | XS4 | 29.1 | 1.2 | 2.9 | 1.1 | 0.061 | 0.06 | 0.03 | 0.03–0.11 | 0.06 | 0.03 |
| Convective | Post-flood | XS5 | 12.9 | 0.6 | 1.6 | 0.6 | 0.061 | 0.07 | 0.02 | 0.04–0.12 | | |
| Convective | Post-flood | XS8 | 23.2 | 1.4 | 2.2 | 1.3 | 0.093 | 0.06 | 0.03 | 0.03–0.13 | | |
| Mesoscale | Pre-flood | XS2 | 7.8 | 0.4 | 0.8 | 0.4 | 0.044 | 0.05 | 0.03 | 0.03–0.11 | | |
| Mesoscale | Pre-flood | XS7 | 1.3 | 0.4 | 0.8 | 0.3 | 0.097 | 0.08 | 0.04 | 0.04–0.16 | | |
| Mesoscale | Pre-flood | XS9 | 7.2 | 0.5 | 1.0 | 0.5 | 0.070 | 0.06 | 0.03 | 0.03–0.13 | 0.06 | 0.03 |
| Mesoscale | Pre-flood | XS10 | 10.4 | 0.8 | 1.4 | 0.8 | 0.090 | 0.07 | 0.03 | 0.03–0.13 | | |
| Mesoscale | Post-flood | XS2 | 9.7 | 0.5 | 0.9 | 0.5 | 0.059 | 0.06 | 0.03 | 0.04–0.12 | | |
| Mesoscale | Post-flood | XS7 | 2.7 | 0.7 | 1.3 | 0.5 | 0.078 | 0.08 | 0.03 | 0.04–0.14 | | |
| Mesoscale | Post-flood | XS9 | 11.7 | 0.8 | 1.4 | 0.7 | 0.064 | 0.07 | 0.03 | 0.04–0.12 | 0.07 | 0.03 |
| Mesoscale | Post-flood | XS10 | 14.9 | 1.2 | 2.6 | 0.9 | 0.086 | 0.07 | 0.03 | 0.03–0.13 | | |

## Estimated peak flows – Critical flow method

The critical flow method yielded estimated peak flows for the convective flood of 31 to 100 $m^3 s^{-1}$ (3.7 to 16 $m^3 s^{-1} km^{-2}$) (Table III; Figure 8). Excluding XS5 range is from 51 to 100 $m^3 s^{-1}$ (5.6 to 16 $m^3 s^{-1} km^{-2}$). These values are 18–35% lower than the corresponding peak flows estimated using the slope-area method, and the pattern of estimated peak flows among the different cross-sections using the critical flow assumption matched the pattern from the slope-area method. Uncertainties were 38 to 140 $m^3 s^{-1}$ (4.5 to 16 $m^3 s^{-1} km^{-2}$), depending on the cross-section (Table III).

Using the critical flow method, estimated mesoscale flood peak flows were all smaller than the estimated peak flows for the convective flood; this is consistent with the results of the slope-area method (Table III). Excluding XS7 on Tributary 3, the estimated peak flows using pre-flood topography varied from 16 to 30 $m^3 s^{-1}$, while the peak flows per unit area varied from 1.8 to 6.5 $m^3 s^{-1} km^{-2}$. Uncertainties were 25 to 87 $m^3 s^{-1}$ (2.7 to 17 $m^3 s^{-1} km^{-2}$). Using the post-flood topography increased the estimated peak flows from 1.4 to 2.8 times, and this was due primarily again to the greater channel cross-sectional area (Table II). Excluding XS7 on Tributary 3, the estimated peak flows using post-flood topography varied from 22 to 51 $m^3 s^{-1}$, while the peak flows per unit area varied from 2.5 to 11 $m^3 s^{-1} km^{-2}$. Uncertainties were 51 to 74 $m^3 s^{-1}$ (5.7 to 15 $m^3 s^{-1} km^{-2}$).

Using the assumed Froude number of 1.0 allowed us to independently estimate Manning's *n* using Equation (2). Resulting *n* values range from 0.058 to 0.097, 0.056 to 0.090, and 0.065 to 0.083 for the convective flood topography, pre-mesoscale flood topography, and post-mesoscale flood topography, respectively.

**Table III.** Comparison of the estimated peak flows using the slope-area method, critical flow method, and Nays2D for the post-convective flood topography and the mesoscale flood using pre-and post-flood topography, respectively. Values in parentheses are the estimated ranges of peak flows per unit area. Uncertainty for the slope-area and critical flow methods was calculated by Gaussian error propagation, and for Nays2D by simulations using the uncertainties in Mannings's *n* and HWMs (see text for details)

| | | | Slope-area in $m^3/s$ ($m^3/s\ km^2$) | | Critical flow in $m^3/s$ ($m^3/s\ km^2$) | | Nays2D in $m^3/s$ ($m^3/s\ km^2$) | |
|---|---|---|---|---|---|---|---|---|
| **Flood** | **Topography** | **Cross-section** | **Peak flow** | **Uncertainty** | **Peak flow** | **Uncertainty** | **Peak flow** | **Uncertainty range** |
| Convective | Post-flood | XS2 | 62 (6.9) | 35 (3.9) | 51 (5.6) | 22 (2.5) | | |
| Convective | Post-flood | XS3 | 140 (16) | 76 (8.6) | 100 (11) | 43 (4.8) | | |
| Convective | Post-flood | XS4 | 140 (16) | 78 (8.9) | 99 (11) | 41 (4.7) | | |
| Convective | Post-flood | XS5 | 32 (3.8) | 13 (1.6) | 31 (3.7) | 15 (1.8) | | |
| Convective | Post-flood | XS8 | 130 (25) | 66 (13) | 85 (16) | 35 (6.8) | 130 (28) | 90–210 (20–46) |
| Mesoscale | Pre-flood | XS2 | 16 (1.8) | 9.7 (1.1) | 16 (1.8) | 8.5 (0.9) | | |
| Mesoscale | Pre-flood | XS7 | 2.5 (0.9) | 1.4 (0.5) | 2.6 (0.9) | 1.4 (0.5) | | |
| Mesoscale | Pre-flood | XS9 | 19 (3.7) | 11 (2.2) | 16 (3.1) | 8.0 (1.6) | | |
| Mesoscale | Pre-flood | XS10 | 40 (8.7) | 21 (4.6) | 30 (6.5) | 13 (2.8) | 20 (2.3) | 10–40 (1.1–4.6) |
| Mesoscale | Post-flood | XS2 | 23 (2.5) | 11 (1.2) | 22 (2.5) | 11 (1.2) | | |
| Mesoscale | Post-flood | XS7 | 6.3 (2.2) | 2.8 (1.0) | 7.3 (2.6) | 3.3 (1.2) | | |
| Mesoscale | Post-flood | XS9 | 34 (6.7) | 14 (2.8) | 33 (6.5) | 15 (2.9) | | |
| Mesoscale | Post-flood | XS10 | 60 (13) | 28 (6.0) | 51 (11) | 21 (4.6) | 50 (5.7) | 20–70 (2.3–8.0) |

### Estimated peak flows - Nays2D modeling

Predicted peak flow for the convective flood using Nays2D and the reach-averaged Manning's *n* was $130\ m^3\ s^{-1}$ (Table III). Peak flow per unit area using the contributing area at the top of the modeled domain, $4.6\ km^2$, was $28\ m^3\ s^{-1}\ km^{-2}$. This discharge is very similar to the values of $130–140\ m^3\ s^{-1}$ calculated from the majority of the cross-sections using the slope-area method. Uncertainty in peak flow ranged from 90 to $210\ m^3\ s^{-1}$, or $20–46\ m^3\ s^{-1}\ km^{-2}$, as a result of incorporating the uncertainty in roughness, and lidar and HWM elevations. Differences in elevations between surveyed HWMs and modeled water surface did not show any longitudinal trend, further supporting the assumption that the tributaries provided negligible additional flow.

The estimated peak flow for the mesoscale flood was $20\ m^3\ s^{-1}$ ($2.3\ m^3\ s^{-1}\ km^{-2}$) using pre-flood topography and $50\ m^3\ s^{-1}$ ($5.7\ m^3\ s^{-1}\ km^{-2}$) using post-flood topography (Table III). This large difference is consistent with peak flow estimates using the other two methods, and estimated peak flows for the pre-flood topography are consistent with the values calculated from the other two methods (Figure 8). In contrast, estimated peak flows for the post-flood topography are slightly higher than the best estimates from the other two methods. The uncertainty range of peak flows was 10 to $40\ m^3\ s^{-1}$ (1.1 to $4.6\ m^3\ s^{-1}\ km^{-2}$) using pre-flood topography, and from 20 to $70\ m^3\ s^{-1}$ (2.3 to $8.0\ m^3\ s^{-1}\ km^{-2}$) using post-flood topography (Table III).

Reach average peak stream power for the convective flood was $3500\ W/m^2$, which is three to five times the peak stream power estimates for the mesoscale flood (Table IV). Durations of the convective and mesoscale floods were estimated as 2 and 24 h, respectively. Using these durations total energy expenditure was estimated as 13 000 kilojoules for the convective flood, which was only 25–46% of the total energy expenditure for the mesoscale flood.

## Discussion

### How do peak flows and geomorphic changes compare between the short-duration, convective flood and the long-duration, mesoscale flood?

Both the convective and mesoscale floods in a burned basin caused extensive geomorphic changes, but the pattern, intensity, and duration of the precipitation and resulting peak flows were very different for the two floods. Studies from nearby fires have shown that nearly all of the hillslope erosion and downstream deposition after wildfire is in response to summer thunderstorms (Moody and Martin, 2001a; Benavides-Solorio and MacDonald, 2005; Kunze and Stednick, 2006). Although we do not have a hydrograph for the convective flood, the radar rainfall data strongly indicates that this would have been a large but short-duration peak flow generated by infiltration-excess overland flow. This runoff mechanism and flashy hydrographs have been widely observed from other thunderstorms on the High Park Fire. In contrast, the mesoscale flood generated a smaller peak flow, but the flows were sustained for a much longer period of time, and our pictures and measured data clearly show that this flood caused substantially greater geomorphic changes across a much larger proportion of the valley bottom (Figures 2, 3, and 7; Table I). As one example, an abandoned dirt road that ran from near the bottom of the watershed up to the confluence with Tributary 3 was cut multiple times by the convective flood, while the mesoscale flood almost completely obliterated the road by reworking the valley bottom.

Costa and O'Connor (1995) posited that the energy available for geomorphic change is the time integral of the unit stream power above an alluvial erosion threshold, where others have shown the alluvial erosion threshold to be ~$300\ W/m^2$ (Miller, 1990; Magilligan, 1992). Our observations and calculations indicate that both floods clearly exceeded alluvial erosion thresholds (Figures 2, 3, and 7; Tables I and IV). Our order-of-magnitude estimates of total energy expenditure (Table IV) show that the convective flood produced very high peak unit stream power but relatively low total energy expenditure, while the mesoscale flood had lower peak unit stream power but a much larger total energy expenditure due to its long duration. The peak stream power and total energy expenditure of both floods fall within the range of 'extreme' geomorphic impact floods presented in Magilligan *et al.* (2015), and they illustrate how both flood magnitude and duration play important roles in determining valley geomorphic changes.

### What is the importance of precipitation intensity, bare soils, and sequence of events on peak flows?

Rainfall intensities for the convective storm are very likely too low as there would have been beam blockage from

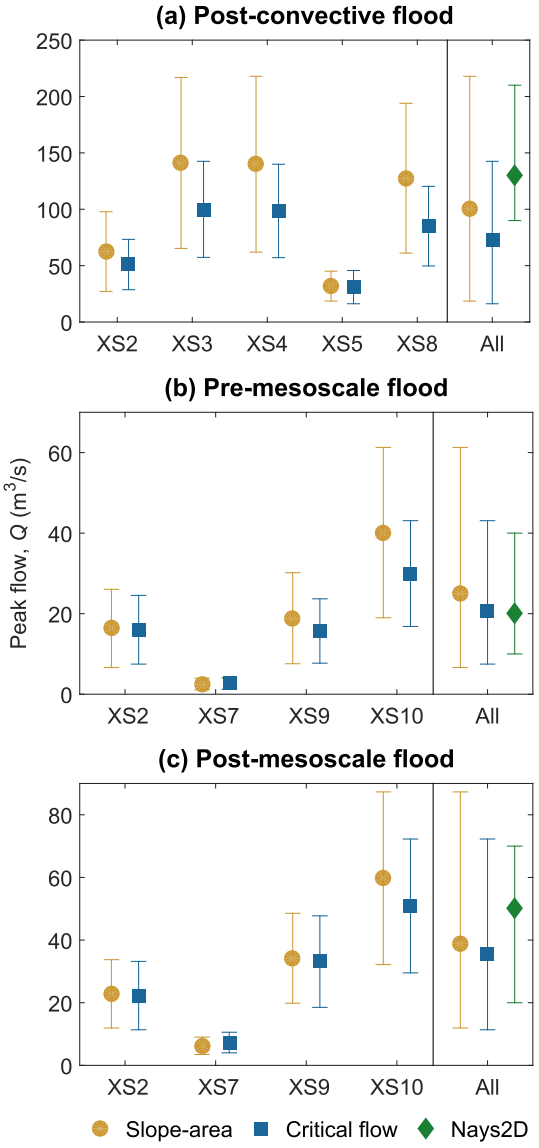


**Figure 8.** Predicted peak flows for each of the three methods for the: (a) convective flood using post-convective flood topography; (b) mesoscale flood using pre-mesoscale flood topography; and (c) mesoscale flood using post-mesoscale flood topography. For the cross-sections the center mark represents the predicted peak flow using the central estimate of Manning's *n*; the vertical bars represent uncertainty. For the 'All' portion of each figure the at-a-station methods represent the average and range from the crosssections. The Nays2D results represent the best estimate using the average Manning's *n* and measured HWM elevations, and the range accounting for uncertainty in Manning's *n*, HWM elevations, and lidar topography (see text for details). Note that XS7 is on Tributary 3 and was not included in the 'All' summary (Figure 4). [Colour figure can be viewed at wileyonlinelibrary.com]

mountainous terrain (Zrnić and Ryzhkov, 1996). Our best estimate of the peak flow for the convective flood on 6 July 2012 using Nays2D is 28 $m^3 s^{-1} km^2$. A simple mass balance assuming no storage shows that an equivalent rainfall intensity of ~100 mm $h^{-1}$ would be needed to generate this flow. Other studies have shown that infiltration immediately after high severity fires in the Colorado Front Range can be less than 10 mm $h^{-1}$ (Moody and Martin, 2001a, b; Kunze and Stednick, 2006; Pietraszek, 2006; Larsen *et al.*, 2009; Schmeer, 2014), so the required peak rainfall intensity is approximately 110 mm $h^{-1}$ or about twice the maximum intensities estimated from the radar data (Figure 5(b)). A maximum intensity of 110 mm $h^{-1}$ for 15 min has an estimated recurrence interval of 25 to 50 years (Perica *et al.*, 2013), which suggests that the July 2012 storm was more extreme than initially conjectured.

From our own observations and those of other researchers, the high flood flow in early July 2012 in SG induced the largest geomorphic changes from any convective storm in a catchment of at least 3 $km^2$ within the HPF. Other thunderstorms did generate more localized peak flows that flooded roads, overtopped culverts, and delivered sediment into the Cache la Poudre River (Writer *et al.*, 2014), but nowhere did anyone note the imbricated boulders and debris deposits shown in Figure 2. The SG convective flood and these other high flows emphasize the dramatic increase in surface runoff, erosion, and peak flows that are common after high and moderate severity fires, particularly in areas subjected to high-intensity convective storms (Moody and Martin, 2001a, b, 2009; Neary *et al.*, 2003; Kunze and Stednick, 2006; Shakesby and Doerr, 2006). The effect of the convective storm was exacerbated by the fact that the most intense rainfall occurred within a month after burning and was concentrated over an area that burned at high severity (Moody and Ebel, 2012).

In contrast, the estimated peak flows from the mesoscale storm were 2–9 $m^3 s^{-1} km^{-2}$ or only 10–30% of the unit area peak flows for the convective flood. The lower estimated peak flows for the mesoscale storm can be explained primarily by the much lower 15 min peak rainfall intensities (Figures 5 and 6). To a lesser extent the lower peak flows from the mesoscale storm also can be attributed to the intervening 15 months of post-fire recovery. In the case of SG, the mean percentage bare soil as measured in 13 or more unmulched swales dropped from 53% in fall 2012 to 42% in fall 2013, and this helped increase the minimum rainfall intensity needed to initiate hillslope-scale erosion from 4 to 9 mm $h^{-1}$ (Schmeer, 2014). By spring 2014 the mean percentage bare soil had dropped to just under 30%, and this means that a storm in summer 2014 similar to the one observed on 6 July 2012 would generate much less runoff and geomorphic changes. Indeed, our field observations confirm that very little channel change has occurred in SG since the September 2013 mesoscale flood, and this is consistent with other studies that have measured the decline in post-fire erosion over time in similar environments (Morris and Moses, 1987; Benavides-Solorio and MacDonald, 2005; Wagenbrenner *et al.*, 2006; Larsen *et al.*, 2009).

The sequence of these two floods in SG also may contribute to the geomorphic changes observed as a result of the mesoscale flood. The convective flood was the first flood after the fire, and this generated large amounts of hillslope and upstream channel erosion, with much of this sediment being deposited on the floodplain below the confluence with Tributary 3

**Table IV.** Estimates of stream power ($W/m^2$) and order-of-magnitude estimates of energy expenditure (kJ), calculated from the Nays2D peak flow estimates (Table III), average wetted width and water surface (WS) slope from the Nays2D models, and estimated flood durations

| Flood | Topography | Peak flow ($m^3/s$) | Width (m) | WS slope (m/m) | Stream power ($W/m^2$) | Duration (hours) | Energy expenditure (kJ) |
|---|---|---|---|---|---|---|---|
| **Convective** | **Post-flood** | 130 | 26 | 0.072 | 3500 | 2 | 13 000 |
| **Mesoscale** | **Pre-flood** | 20 | 19 | 0.062 | 650 | 24 | 28 000 |
| **Mesoscale** | **Post-flood** | 50 | 24 | 0.058 | 1200 | 24 | 51 000 |

(Figure 2(b)). This unconsolidated sediment effectively 'loaded the gun' for the subsequent erosion (sensu Nanson, 1986) during the long-duration mesoscale flood, which removed and transported nearly all of the sediment that had been deposited up to that point (Figures 3 and 7). The short duration of the high-intensity rainfall and large amounts of deposition suggests that the convective flood was more sediment transport capacity limited, while the September flood was eventually more sediment supply-limited because the sustained rainfall and high flows were able to transport all but the coarsest portion of the previously deposited sediment and increase the size of the channel (Figure 3). The sequence of floods can therefore play an important role on the subsequent valley geomorphic changes (Germanoski *et al.*, 2002).

## How precisely can we estimate peak flows for each storm? And can our confidence in the estimated peak flows be improved by using and comparing different estimation techniques?

In this study we compared the peak flows from two storms using the slope-area method, critical flow method, and a 2D hydraulic model (Figure 8). Each peak flow estimation method comes with inherent limitations; for example, uncertainties in estimating roughness plus expansion and contraction losses can lead to errors of 100% or more in the slope-area method (Jarrett, 1987). The critical flow method (Grant, 1997; Webb and Jarrett, 2002; Moody *et al.*, 2008a,b) does not require an estimate of roughness but it sets the Froude number equal to 1.0 while larger values can occur during large floods in steep channels (Costa, 1987; Jarrett, 1987, and references therein). A larger Froude number will result in an underestimate of velocity and discharge, and in our results the estimated peak flows from the critical flow method were consistently lower than the peak flows estimated from the slope-area method and generally lower than Nays2D.

Two-dimensional (2D) hydraulic models are preferred for paleohydrology because these can better quantify downstream and cross-stream patterns of flow depth, velocity and shear stress (Nelson *et al.*, 2003; Morvan *et al.*, 2008) with a resulting increase in accuracy (Hicks *et al.*, 2005; Smith et al., 2005a, b; Tonina and Jorde, 2013). The primary drawback to 2D models is they require detailed topography that can be difficult to acquire; however, this is quickly becoming less of an issue as high resolution topography becomes available (Passalacqua *et al.*, 2015). The peak flow estimates using Nays2D were very consistent with the median values from the slope-area method for the convective storm and the mesoscale flood using pre-flood topography. The uncertainty range in Nays2D was generally larger than the uncertainty for the other two methods when compared with the uncertainty at a single cross-section. However, the uncertainty of the peak flow estimates using Nays2D is less than the uncertainty that results from the large differences in the estimated peak flows among the different cross-sections (Figure 8, 'All'). This suggests that the ability to integrate estimates from different cross-sections and HWMs in a 2D model can reduce the overall uncertainty for estimating peak flows after a large flood.

Common but often unrecognized problems for estimating peak flows after floods are that they implicitly assume: (1) high-water marks (HWMs) accurately represent the water surface profile during the peak flow; and (2) the post-flood bed topography and other parameters such as surface roughness are representative of the conditions when the HWMs were established. It is clear that accurate *a posteriori* estimates of peak flows are directly related to the accuracy of the HWMs (House and Pearthree, 1994; Jarrett and England, 2002), but we believe that the elevations of our HWMs are quite accurate given the fineness of the debris lines and the accuracy of our surveys. A potentially much greater source of error is that floods often cause extensive deposition or incision (Costa and O'Connor, 1995; Elliott and Parker, 2001; Hicks *et al.*, 2005), and the timing of topographic channel change relative to the establishment of the HWMs is nearly impossible to determine. The resulting uncertainties in peak flows due to channel change are typically ignored in indirect peak flow calculations (Lumbroso and Gaume, 2012), but the magnitude of erosion and deposition – particularly after moderate to severe wildfires – indicates that intra-event channel change can be a major source of uncertainty for indirect peak flow estimates. Large uncertainties in estimating peak flows also are introduced when cross-sections and HWMs are widely spaced, differences between cross-sections exist (inundated area and local slopes), and there is much uncertainty in roughness (Tables I and II). Additional sources of uncertainty among cross-sections could be due to possible inflows, transmission losses, and hydrodynamic dispersion, but our results indicate that the two largest sources of uncertainty are the uncertainty in roughness and the intra-event changes in bed topography, which we discuss below.

The uncertainty in roughness generally receives the most attention in studies attempting to make indirect estimates of large flood peaks (Costa, 1987; Wohl, 1998). Our results show that the effect of this uncertainty in roughness varies greatly according to the technique being used. Peak flows estimated by the slope-area method are most affected by the uncertainty in roughness because the calculated discharge is inversely proportional to Manning's $n$ (Equation (1)). The coefficient of variation of our Manning's $n$ estimates ranges from 36% to 55% depending on the specific cross-section and the topography, which exceeds the 25% uncertainty suggested by Wohl (1998). The uncertainty in Manning's $n$ stems primarily from lumping all forms of resistance (e.g. grain roughness, form drag due to bedforms and channel geometry, vegetation resistance, as well as added fluid resistance due to sediment transport) into a single roughness parameter (Trieste and Jarrett, 1987; Lumbroso and Gaume, 2012). Field guides and empirical equations have been developed to facilitate more accurate estimates of Manning's $n$, but these often perform poorly in small mountain streams (Marcus *et al.*, 1992; Smith *et al.*, 2007; Ferguson, 2010; Mrokowska *et al.*, 2014) as evidenced by the wide range of Manning's $n$ values estimated by these different methods for our reach (0.03 to 0.13, excluding XS7).

Manning's $n$ values can be back-calculated from direct discharge measurements, but baseflows in SG are only a couple of decimeters deep, making the extrapolation of a Manning's $n$ to large floods very difficult given that it varies with stream stage (Lee and Ferguson, 2002; Reid and Hickin, 2008; Ferguson, 2010; Yochum *et al.*, 2014). Direct discharge measurements during larger flows are often extremely difficult because the largest post-fire floods in our region are generated by short-duration localized thunderstorms. Uncertainty in the location of and timing of these storms, the lack of ready access, and the flashiness of the flood response makes it highly unlikely that such peak flows can be directly measured.

Momentum extraction due to resistance from the large-scale roughness of bedforms and nonuniform channel geometry are more accurately represented in a 2D model than in 1D or at-a-station calculations (Morvan *et al.*, 2008). Thus, 2D model predictions are less sensitive to the specific choice of $n$ for small-scale roughness (i.e. grain resistance). The reduced sensitivity to $n$ is a major rationale for using a more sophisticated and physically-based technique than the slope-area method.

Most estimates of peak flows do not have the data, or do not attempt to determine, the effects of changes in channel topography on the estimated peak flows. In our study the mesoscale flood increased the cross-sectional areas by a minimum of 24% at XS2 to more than 60% at XS9. Local slopes changed from −20% at XS7 to +34% at XS2 (Table II), with the changes in slope being primarily due to the establishment and movement of local knickpoints (sensu Gardner, 1983). All of the tributaries also incised due to the sustained high flows and lower base level in the mainstem of SG during the mesoscale flood. Our results show that these changes in cross-sectional area and local slope can cause a similar or larger percentage change in the estimated peak flows than the uncertainties in roughness and HWM elevation (Table III; Figure 8). More specifically, there was approximately a two-fold difference in the estimated peak flow for the mesoscale flood when using the slope-area and critical flow method, depending on whether we used the pre- or the post-flood topography. Similarly, the calculated peak flow using Nays2D increased from 20 $m^3 s^{-1}$ using the pre-flood topography to 50 $m^3 s^{-1}$ using the post-flood topography, and this difference of 30 $m^3 s^{-1}$ is larger than the uncertainty for either the pre- or post-flood estimates.

The true peak flow for the mesoscale flood is probably between the values calculated using pre- and post-flood topography, but there is no way to determine the precise bed topography at the time of highest discharge. For the convective flood we are in the more common position of only having post-flood topography. Field observations in our reaches indicate that the convective flood was primarily depositional, so the cross-sectional area during the highest flow would have been at least equal to or greater than the measured post-flood cross-section. This would suggest that the true peak flow was probably larger than our estimated values in Table III. We posit that post-flood topography would more accurately estimate the peak flow from an incising flood than a depositional flood, as stream power and erosion are likely greatest at the peak flow. This would mean that the peak flows for the mesoscale flood are more accurately represented by the post-flood topography.

For a depositional flood the post-flood topography is more likely to underestimate the peak flow due to sediment deposition during the falling limb of the hydrograph. While a depositional flood could have initial scour, this is unlikely given the usual tendency for peak sediment concentrations and higher sediment transport rates to be on the rising limb of a hydrograph (Walling, 1977; Hsu *et al.*, 2011). An incising flood is very unlikely to have an initial depositional phase, and this again would suggest that post-flood topography provides a more accurate estimate of peak flows for incising than depositional floods. Many floods also have multiple peaks and this, plus the complexities of varying sediment sources and supplies, means that all estimates of peak flows based on post-flood topography have a relatively high degree of uncertainty that is typically ignored.

The discussion above indicates that the slope-area method will have the greatest uncertainty because it is sensitive to the assumed Manning's $n$ value as well as the assumption that the cross-sectional areas and slopes measured after a flood reflect the conditions at the time of the highest instantaneous flow. Our results for the mesoscale flood did show an unexpected decrease in some of the central estimates for the slope-area peak flows with increasing drainage area (Table III); however, with the exception of XS5 for the convective flood (where the HWM elevation was likely underestimated) and XS7 for the mesoscale flood (which was on a tributary), the uncertainty envelopes among the different cross-sections overlap (Figure 8). This illustrates the importance of quantifying uncertainty, which can be quite large, in these types of calculations.

The critical flow method does not require an estimate of roughness, but it necessarily assumes that the Froude number is 1.0 and any deviation from this assumption has a corresponding effect on the calculated peak flows. Costa (1987) noted that the Froude number can greatly exceed 1.0 for large floods in steep channels, and this will lead to a severe underestimate of peak flows. Grant (1997) suggested that peak flows tend to asymptotically approach critical flow as slope increases in threshold channels, but the 2 m piles of debris against standing trees, the elevations of the HWMs, and the estimated peak flows clearly suggest the convective flood was a very exceptional flood and the Froude numbers likely exceeded 1.0 at least around the time of the peak flow.

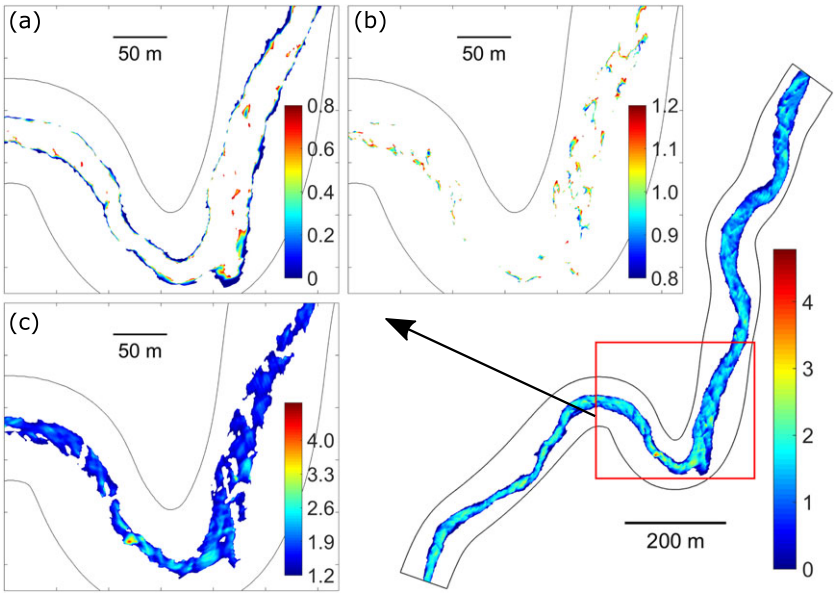


**Figure 9.** Predicted Froude numbers from Nays2D for the convective flood using $n = 0.06$ and $Q = 130$ $m^3/s$. The entire model reach is shown in the lower right, and the highlighted reach in a-c is centered around XS6 and XS8. (a) Areas with Froude numbers below 0.80, (b) areas with Froude numbers from 0.8 to 1.2, and (c) areas with Froude numbers greater than 1.2. [Colour figure can be viewed at wileyonlinelibrary.com]

An important benefit of using the Nays2D model is that it can be used to check on the validity of the critical flow method because it provides location-specific Froude values. Our simulation for the convective flood using $n = 0.06$ and the associated best-fit discharge of 130 $m^3 s^{-1}$ shows that much of the channel had Froude numbers greater than 1.2 (Figure 9). The potential for higher Froude numbers at peak discharge during the convective flood is also supported by the results in Table III, as the estimated peak flows from the critical flow method were generally lower than the peak flows calculated with the slope-area method and Nays2D.

The uncertainties in roughness, topography and Froude number suggest that 2D modeling should be used for indirect estimates of peak flows when possible, and a combination of methods is the best approach as they can be compared and help support or reject certain values and assumptions. As noted above, our results from Nays2D led us to question the basic assumption in the critical flow method (Figure 9). On the other hand, the critical flow method provided 11 independent estimates of main channel roughness (excluding XS7) for the three peak flows, which can help inform the potential validity of different roughness values for the slope-area method. Hence a full assessment of the range and likely uncertainty in peak flow estimates requires the use of multiple estimation techniques, a range of input parameters, multiple cross-sections, and measured or estimated changes in channel topography. A comparison of the results from different locations and methods using different assumptions can help identify and cross-check the most likely range of values rather than estimating a single specific value (Legleiter *et al.*, 2011).

## How do these floods compare to other large rainfall-runoff generated floods in the United States?

The convective flood was an exceptionally large flood. Estimated peak flows of 90–210 $m^3 s^{-1}$ from Nays2D for the convective flood fall along the 99th percentile curve for the largest rainfall-runoff floods for similar-sized watersheds in the United States and Puerto Rico (Figure 10; O'Connor and Costa, 2004). Few floods of this magnitude have been observed in the central Rocky Mountains United States (Figure 10, inset), and most of the floods from drainage basins smaller than 100 $km^2$ are from the interior west and were caused by isolated convective storms (O'Connor and Costa, 2004). The estimated peak flow of 50 $m^3 s^{-1}$ for the post-mesoscale flood topography falls just below the 90th percentile compared with other rainfall-runoff floods in the US and Puerto Rico (Figure 10). Our estimated peak flow per unit drainage area (5.7 $m^3 s^{-1} km^{-2}$) for the mesoscale flood is generally consistent with many other estimates from the Colorado Front Range during the mesoscale storm (Yochum and Moore, 2013; Moody, 2016), although Yochum and Moore's (2013) estimate from SG of 7.9 $m^3 s^{-1} km^{-2}$ is 1.4 times greater than our best estimate of peak flows from Nays2D. The use of a 2D model in conjunction with multiple HWMs at different locations provides a more robust method of estimating peak flows, suggesting that Yochum and Moore's (2013) peak flow assessment for the mesoscale flood is likely an overestimate.

Geomorphic changes from the two floods studied in this paper are still very evident years later. The imbricated boulders, piled woody debris, and some of the higher elevation and particularly coarse sediment deposits from the convective flood

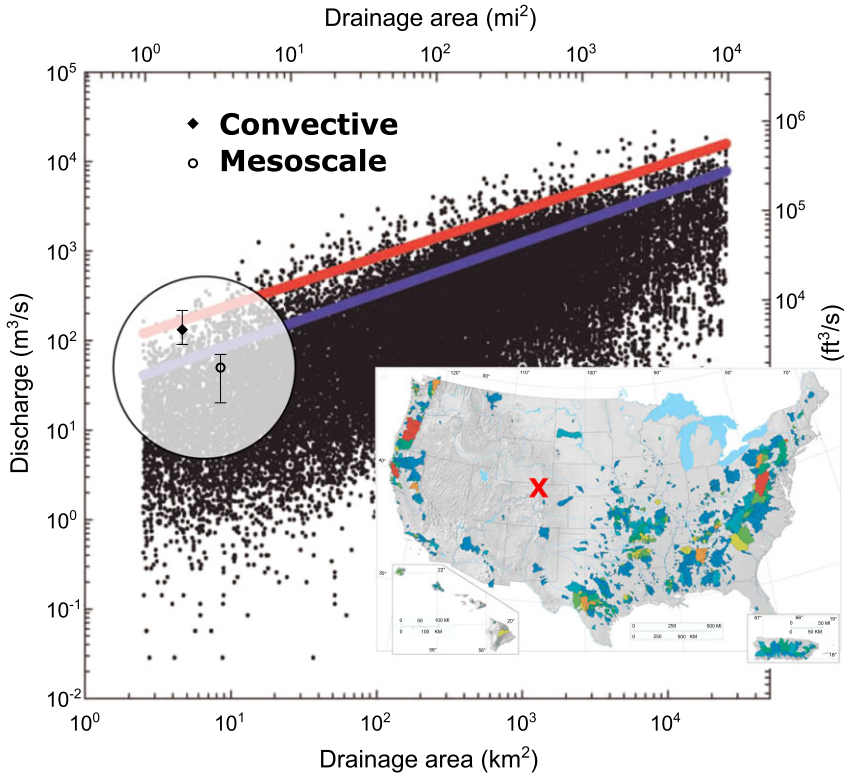


**Figure 10.** Plot of the largest rainfall-runoff floods experienced in the United States and Puerto Rico (modified from O'Connor and Costa, 2004) with the diamond and open circle showing the predicted peak flows from Nays2D model for the convective flood (130 $m^3/s$) and the mesoscale flood (50 $m^3/s$) using post-flood topography, respectively. Vertical bars represent the range of estimated peak flow for the convective flood (90–210 $m^3/s$) and the mesoscale flood (20–70 $m^3/s$). The watershed areas for the convective flood (4.6 $km^2$) and the mesoscale flood (8.7 $km^2$) are different due to the different model domains used to predict each flow with Nays2D. The diagonal blue and red lines correspond to the ~90th and ~99th percentiles, respectively. Inset map shows the locations of watersheds contributing to the ~90th percentile, and the red X indicates the location of Skin Gulch. [Colour figure can be viewed at wileyonlinelibrary.com]

are still present. The mesoscale flood reworked both the post-fire and historic valley fill deposits, and there have been minimal geomorphic changes to the channel or valley bottom since that flood. Given the continuing vegetative recovery and associated reductions in hillslope runoff and erosion, further channel geomorphic changes are unlikely and these two floods have largely reset the system compared with pre-fire conditions.

There are few data on the frequency of large-magnitude floods following fires in the Colorado Front Range, but charcoal deposits from incised channels indicate a 900–1000 year recurrence interval for fires and floods (Elliott and Parker, 2001) with the potential for even greater timespans (Cotrufo *et al.*, 2016). Since we are unaware of other watersheds in the High Park fire that experienced comparable flooding and geomorphic changes as observed from the convective flood in Skin Gulch, we posit that the post-fire flood deposits and channel change in Skin Gulch constitute a near millennium-scale event. In a stationary world this sequence of severe, basin-scale forest fire and subsequent extreme runoff can cause an aggradational signature that persists for centuries (Hamilton *et al.*, 1954; Meyer *et al.*, 1992, 1995; Moody and Martin, 2001a; Legleiter *et al.*, 2003). But in our non-stationary world with increased temperatures, earlier snowmelt, and a shift from snow to rain (Clow, 2010; Liu *et al.*, 2013; Rocca *et al.*, 2014), resource managers and the public must be prepared for more of these severe fire–flood events.

## Conclusions

Our investigation of two extreme floods that occurred after the Skin Gulch watershed burned in the 2012 High Park Fire shows how precipitation characteristics, burn severity, and time since burning are important controls on peak flows and geomorphic changes in a burned landscape. The convective flood on 6 July 2012 was just one week after burning, when a brief (~2 h) but intense convective summer thunderstorm focused over an area of high burn severity, produced a very large flood (~130 $m^3 s^{-1}$) with high peak unit stream power (3500 $W/m^2$) and extensive downstream deposition. The mesoscale flood in September 2013 was from an exceptionally long duration mesoscale storm, which produced a smaller flood peak (~20–50 $m^3 s^{-1}$), but the long duration (~24 h), and subsequently more total energy expenditure, caused channel incision and widening through extensive reworking of both recent and pre-existing valley bottom alluvial deposits.

Uncertainty in estimates of channel roughness, measured high-water mark elevations, and remotely sensed topographic data led to considerable uncertainties in the estimated peak flows for both floods. Slope-area estimates had the greatest uncertainty due in large part to the uncertainty in Manning's roughness. Estimated peak flows from the critical flow method were generally lower because the assumed Froude number of 1.0 set an upper limit on the estimated peak flows. The 2D model was less sensitive to the assumed roughness, although uncertainty in high-water mark elevations and airborne lidar topography still led to a wide range of peak flow estimates. Our peak flow estimates for the mesoscale flood varied by roughly a factor of two depending on whether we used pre- or post-flood topography, and this indicates that the inherent uncertainty in the amount and timing of intra-event channel change can have an even larger effect on estimated peak flows than the uncertainty in roughness.

The estimated peak flow of 130 $m^3 s^{-1}$ (28 $m^3 s^{-1} km^{-2}$) for the convective flood is among the largest floods per unit area observed in the United States, and this illustrates the profound effect of brief but intense precipitation over areas recently burned at high severity. The lower peak discharge of 50 $m^3 s^{-1}$ (5.7 $m^3 s^{-1} km^{-2}$) for the mesoscale flood is attributed primarily to the lower peak rainfall intensities and secondarily to post-fire recovery. However, this flood was geomorphically much more effective due to the long duration of high flows and the large amount of sediment deposited after the fire from previous storms. Climate change indicates that fire-induced floods will become more common in the future; both the magnitudes of peak flows and the methodological implications from this study can help guide resource managers and future post-flood analyses.

*Acknowledgements*—We thank Steven Filippelli, Jacob Morgan, Sarah Schmeer, and Brandon Stone for providing data and valuable insight on data analysis. James Smith and Mary Lynn Baeck graciously provided Hydro-NEXRAD data, and we thank Ellen Wohl for her feedback on our work. We are very grateful to so many others that helped collect field data. Comments from three reviewers and the Associate Editor improved the clarity of this manuscript. This research was supported by National Science Foundation grants EF-1250205, EF-1339928, and EAR-1419223, and USDA National Institute of Food and Agriculture Hatch project 1003276. Airborne LiDAR used in this analysis was provided by the National Ecological Observatory Network, a project sponsored by the National Science Foundation and managed under cooperative agreement by NEON, Inc. This material is based in part upon work supported by the National Science Foundation under Grant No. DBI-0752017.

## References

Abbott JT. 1970. Geology of precambrian rocks and isotope geochemistry of shear zones in the Big Narrows Area, northern Front Range, Colorado. US Geological Survey Open-File Report 70–1: Denver, CO; 239.

Anderson HW. 1976. Fire effects on water supply, floods, and sedimentation. In *Proceedings of the Annual Tall Timbers Fire Ecology Conference* 15, Portland, OR; Tallahassee, FL, 16–17 October 1974: 249–260.

Anderson SW, Anderson SP, Anderson RS. 2015. Exhumation by debris flows in the 2013 Colorado Front Range storm. *Geology* **43**(5): 391–394.

Arcement GJJ, Schneider VR. 1989. Guide for selecting Manning's roughness coefficients for natural channels and flood plains. US Geological Survey Water-Supply Paper 2339: Denver, CO; 38.

Asahi K, Shimizu Y, Nelson J, Parker G. 2013. Numerical simulation of river meandering with self-evolving banks. *Journal of Geophysical Research: Earth Surface* **118**: 1–22.

Barnes HH. 1967. Roughness characteristics of natural channels. US Geological Survey Water-Supply Paper 1849: Washington DC; 213.

Benavides-Solorio JD, MacDonald LH. 2005. Measurement and prediction of post-fire erosion at the hillslope scale, Colorado Front Range. *International Journal of Wildland Fire* **14**(4): 457–474.

Canfield HE, Wilson CJ, Lane LJ, Crowell KJ, Thomas WA. 2005. Modeling scour and deposition in ephemeral channels after wildfire. *Catena* **61**: 273–291.

Cannon SH, Kirkham RM, Parise M. 2001. Wildfire-related debris-flow initiation processes, Storm King Mountain, Colorado. *Geomorphology* **39**: 171–188.

Chow VT. 1959. *Open-Channel Hydraulics*. McGraw-Hill Book Co: New York; 680.

Cifelli R, Doesken N, Kennedy P, Carey LD, Rutledge SA, Gimmestad C, Depue T. 2005. The community collaborative rain, hail, and snow network: informal education for scientists and citizens. *Bulletin of the American Meteorological Society* **86**: 1069–1077.

Clow DW. 2010. Changes in the timing of snowmelt and streamflow in Colorado: a response to recent warming. *Journal of Climate* **23**: 2293–2306.

Costa JE. 1987. Hydraulics and basin morphometry of the largest flash floods in the conterminous United States. *Journal of Hydrology* **93**: 313–338.

Costa JE. 1988. Rheologic, geomorphic, and sedimentologic differentiation of water floods, hyperconcentrated flows, and debris flows. In *Flood Geomorphology*, Baker VR, Kochel RC, Patton PC (eds). Wiley-Interscience: New York; 113–122.

Costa JE, O'Connor JE. 1995. Geomorphically effective floods. In *Natural and Anthropogenic Influences in Fluvial Geomorphology, Geophysical Monograph*, Vol. **89**. AGU: Washington, DC; 45–56.

Cotrufo MF, Boot CM, Kampf S, Nelson PA, Brogan DJ, Covino T, Haddix ML, MacDonald LH, Rathburn S, Ryan-Bukett S, Schmeer S, Hall E. 2016. Redistribution of pyrogenic carbon from hillslopes to stream corridors following a large montane wildfire. *Global Biogeochemical Cycles* **30**: 1–8.

Dalrymple T, Benson MA. 1967. Measurement of Peak Discharge by the Slope-area Method. US Geological Survey Techniques of Water-Resources Investigations, Book 3, Chapter A2, Washington, DC: 12.

Dingman SL, Sharma KP. 1997. Statistical development and validation of discharge equations for natural channels. *Journal of Hydrology* **199**: 13–35.

Doehring DO. 1968. The effect of fire on geomorphic processes in the San Gabriel Mountains, California. In *Contributions to Geology*, Parker RB (ed). University of Wyoming: Laramie; 43–65.

Eaton BC, Giles TR. 2008. Assessing the effect of vegetation-related bank strength on channel morphology and stability in gravel-bed streams using numerical model. *Earth Surface Processes and Landforms* **34**: 712–724.

Ebel BA, Moody JA, Martin DA. 2012. Hydrologic conditions controlling runoff generation immediately after wildfire. *Water Resources Research* **48**: 1–13.

Elliott JG, Parker RS. 2001. Developing a post-fire flood chronology and recurrence probability from alluvial stratigraphy in the Buffalo Creek watershed, Colorado, USA. *Hydrological Processes* **15**: 3039–3051.

Ferguson R. 2007. Flow resistance equations for gravel- and boulder-bed stream. *Water Resources Research* **43**: 1–12.

Ferguson R. 2010. Time to abandon the Manning equation? *Earth Surface Processes and Landforms* **35**: 1873–1876.

Flannigan MD, Krawchuk MA, de Groot WJ, Wotton BM, Gowman LM. 2009. Implications of changing climate for global wildland fire. *International Journal of Wildland Fire* **18**: 483–507.

Gardner TW. 1983. Experimental study of knickpoint and longitudinal profile evolution in cohesive, homogeneous material. *Geological Society of America Bulletin* **94**: 664–672.

Germanoski D, Miller JR, Latham DD. 2002. The importance of event sequencing on the geomorphic impact of wildfire in the central Great Basin. *Geological Society of America Abstracts with Programs* **34**: 319.

Gochis D, Schumacher R, Friedrich K, Doesken N, Kelsch M, Sun J, Ikeda K, Lindsey D, Wood A, Dolan B, Matrosov S, Newman A, Mahoney K, Rutledge S, Johnson R, Kucera P, Kennedy P, Sempere-Torres D, Steiner M, Roberts R, Wilson J, Yu W, Chandrasekar V, Rasmussen R, Anderson A, Brown B. 2014. The Great Colorado Flood of September 2013. *Bulletin of the American Meteorological Society*. https://doi.org/10.1175/BAMS-D-13-00241.1.

Grant GE. 1997. Critical flow constrains flow hydraulics in mobile-bed streams: a new hypothesis. *Water Resources Research* **33**: 349–358.

Hamilton EL, Horton JS, Rowe PB, Reimann LF. 1954. Fire-flood Sequences on the San Dimas Experimental Forest. USDA Forest Service, California Forest and Range Experiment Station Technical Paper No.6: Berkeley, CA; 29.

Hey RD. 1979. Flow resistance in gravel bed rivers. *Journal of the Hydraulics Division, American Society of Civil Engineers* **105**(HY4): 365–379.

Hicks NS, Smith JA, Miller AJ, Nelson PA. 2005. Catastrophic flooding from an orographic thunderstorm in the central Appalachians. *Water Resources Research* **41** W12428.

House PK, Pearthree PA. 1994. A geomorphologic and hydraulic evaluation of an extraordinary flood discharge estimate: Bronco Creek, Arizona. Arizona Geological Survey Open-File Report 94–19: Tucson, Arizona; 21.

HPF BAER Report (High Park Fire Burned Area Emergency Response Report). 2012. Department of Transportation, Larimer County, Natural Resources Conservation Service, US Forest Service; 25.

Hsu L, Finnegan NJ, Brodsky EE. 2011. A seismic signature of river bedload transport during storm events. *Geophysical Research Letter* **38** L13407, doi:https://doi.org/10.1029/2011GL047759.

Jarrett RD. 1984. Hydraulics of high-gradient streams. *Journal of Hydraulic Engineering* **110**(11): 1519–1539.

Jarrett RD. 1987. Errors in slope-area computations of peak discharges in mountain streams. *Journal of Hydrology* **96**: 53–67.

Jarrett RD, England JF, Jr. 2002. Reliability of paleostage indicators for paleoflood studies. In *Ancient Floods, Modern Hazards*, House PK, Webb RH, Baker VR, Levish DR (eds). American Geophysical Union: Washington, DC; 91–109.

Jin S, Yang L, Danielson P, Homer C, Fry J, Xian G. 2013. A comprehensive change detection method for updating the National Land Cover Database to circa 2011. *Remote Sensing of Environment* **132**: 159–175.

Kampf SK, Brogan DJ, Schmeer S, MacDonald LH, Nelson PA. 2016. How do geomorphic effects of rainfall vary with storm type and spatial scale in a post-fire landscape? *Geomorphology* **273**: 39–51.

Krajewski WF, Kruger A, Smith JA, Lawrence R, Gunyon C, Goska R, Seo BC, Domaszczynski P, Baeck ML, Ramamurthy MK, Weber J, Bradley AA, DelGreco SA, Steiner M. 2011. Towards better utilization of NEXRAD data in hydrology: an overview of Hydro-NEXRAD. *Journal of Hydroinformatics* **13**(2): 255–266.

Kunze MD, Stednick JD. 2006. Streamflow and suspended sediment yield following the 2000 Bobcat fire, Colorado. *Hydrological Processes* **20**: 1661–1681.

Larsen IJ, MacDonald LH, Brown E, Rough D, Welsh MJ, Pietraszek JH, Libohova Z, Benavides-Solorio J, Schaffrath K. 2009. Causes of post-fire runoff and erosion: water repellency, cover, or soil sealing? *Soil Science Society of America Journal* **73**: 1393–1407.

Lee AJ, Ferguson RI. 2002. Velocity and flow resistance in step-pool streams. *Geomorphology* **46**: 59–71.

Legleiter CJ, Kyriakidis PC, McDonald RR, Nelson JM. 2011. Effects of uncertain topographic input data on two-dimensional flow modeling in a gravel-bed river. *Water Resources Research* **47** W03518.

Legleiter CJ, Lawrence RL, Fonstad MA, Marcus WA, Aspinall R. 2003. Fluvial response a decade after wildfire in the northern Yellowstone ecosystem: a spatially explicit analysis. *Geomorphology* **54**: 119–136.

Limerinos JT. 1970. Determination of the Manning coefficient from measured bed roughness in natural channels. US Geological Survey Water-Supply Paper 1898-B: Washington, DC; 47.

Littell JS, McKenzie D, Peterson DL, Westerling AL. 2009. Climate and wildfire area burned in western US ecoprovinces, 1916–2003. *Ecological Applications* **19**(4): 1003–1021.

Liu YQ, Goodrick SL, Stanturf JA. 2013. Future US wildfire potential trends projected using a dynamically downscaled climate change scenario. *Forest Ecology and Management* **294**: 120–135.

Lukas J, Wolter K, Mahoney K, Barsugli J, Doesken N, Ryan W, Rangwala I, Livneh B, Gordon E, Hoerling M, Kiladis G. 2013. Severe flooding on the Colorado Front Range: A preliminary assessment. Western Water Assessment. 4. Retrieved 4 June 2014 from http://coflood2013.colostate.edu/docs/wwa_assessment.pdf.

Lumbroso D, Gaume E. 2012. Reducing the uncertainty in indirect estimates of extreme flash flood discharges. *Journal of Hydrology* **414–415**: 16–30.

Magilligan FJ. 1992. Thresholds and the spatial variability of flood power during extreme floods. *Geomorphology* **5**: 373–390.

Magilligan FJ, Buraas E, Renshaw C. 2015. The efficacy of stream power and flow duration on geomorphic responses to catastrophic flooding. *Geomorphology* **228**: 175–188.

Marcus WA, Roberts K, Harvey L, Tackman G. 1992. An evaluation of methods for estimating Manning's n in small mountain streams. *Mountain Research and Development* **12**(3): 227–239.

Meyer GA, Wells SG, Balling RC, Jr, Jull AJT. 1992. Response of alluvial systems to fire and climate change in Yellowstone National Park. *Nature* **357**: 147–150.

Meyer GA, Wells SG, Jull AJT. 1995. Fire and alluvial chronology in Yellowstone National Park: climatic and intrinsic controls on Holocene geomorphic processes. *Geological Society Of America Bulletin* **107**(10): 1211–1230.

Miller AJ. 1990. Flood hydrology and geomorphic effectiviness in the central Appalachians. *Earth Surface and Processes and Landforms* **15**: 119–134.

Moody JA. 2016. *Estimates of peak flood discharge for 21 sites in the Front Range in Colorado in response to extreme rainfall in September 2013*. Geological Survey Scientific Investigations Report 2016-5003: Reston, Virginia; 64 pp.

Moody JA, Ebel BA. 2012. Hyper-dry conditions provide new insights into the cause of extreme floods after wildfire. *Catena* **93**: 58–63.

Moody JA, Martin DA. 2001a. Initial hydrologic and geomorphic response following a wildfire in the Colorado Front Range. *Earth Surface Processes and Landforms* **26**: 1049–1070.

Moody JA, Martin DA. 2001b. Post-fire, rainfall intensity-peak discharge relations for three mountainous watersheds in the western USA. *Hydrological Processes* **15**: 2981–2993.

Moody JA, Martin DA. 2009. Synthesis of sediment yields after wildland fire in different rainfall regimes in the western United States. *International Journal of Wildland Fire* **18**: 96–115.

Moody JA, Martin DA, Cannon SH. 2008a. Post-wildfire erosion response in two geologic terrains in the western USA. *Geomorphology* **95**: 103–118.

Moody JA, Martin DA, Haire SL, Kinner DA. 2008b. Linking runoff response to burn severity after a wildfire. *Hydrological Processes* **22**: 2063–2074.

Morris SE, Moses TA. 1987. Forest fire and the natural soil erosion regime in the Colorado Front Range. *Annals of the Association of American Geographers* **77**(2): 245–254.

Morvan H, Knight D, Wright N, Tang X, Crossley A. 2008. The concept of roughness in fluvial hydraulics and its formulation in 1D, 2D and 3D numerical simulation models. *Journal of Hydraulic Research* **46** (2): 191–208.

Mrokowska MM, Rowiński PM, Kalinowska MB. 2014. Notes on the estimation of resistance to flow during flood wave propagation. *Hydrologic Earth Systems Science Discussion* **11**: 13311–13352.

Nanson GC. 1986. Episodes of vertical accretion and catastrophic stripping: a model of disequilibrium flood-plain development. *Geological Society of America Bulletin* **97**: 1467–1475.

Neary DG, Gottfried GJ, Ffolliott PF. 2003. Post-wildfire watershed flood responses. In *Proceedings of the Second International Fire Ecology and Fire Management Congress*: Orlando, Florida, 16–20 November 2003, Paper 1B7.

Nelson JM, Bennett JP, Wiele SM. 2003. Flow and sediment-transport modeling. In *Tools in Fluvial Geomorphology*, Kondolf GM, Piegay H (eds). Wiley: Chichester, England; 539–576.

Nelson JM, Shimizu Y, Abe T, Asahi K, Gamou M, Inoue T, Iwasaki T, Kakinuma T, Kawamura S, Kimura I, Kyuka T, McDonald RR, Nabi M, Nakatsugawa M, Simões FR, Takebayashi H, Watanabe Y. 2015. The international river interface cooperative: public domain flow and morphodynamics software for education and applications. *Advances in Water Resources*. https://doi.org/10.1016/j.advwatres.2015.09.017.

O'Connor JE, Costa JE. 2004. Spatial distribution of the largest rainfall-runoff floods from basins between 2.6 and 26,000 $km^2$ in the United States and Puerto Rico. *Water Resource Research* **40** W01107.

Onda Y, Dietrich WE, Booker F. 2008. Evolution of overland flow after a severe forest fire, Point Reyes, California. *Catena* **72**: 13–20.

Parsons A, Robichaud PR, Lewis SA, Napper C, Clark JT. 2010. Field guide for mapping post-fire soil burn severity. USDA Forest Service General RMRS-GTR-243: Fort Collins, CO; 49.

Passalacqua P, Belmont P, Staley DM, Simley JF, Arrowsmith JR, Bode CA, Crosby C, DeLong SB, Glenn NF, Kelly SA, Lague D, Sangireddy H, Schaffrath K, Tarboton DG, Wasklewicz T, Wheaton JM. 2015. Analyzing high resolution topography for advancing the understanding of mass and energy transfer through landscapes: a review. *Earth-Science Reviews* **148**: 174–193.

Perica S, Martin D, Pavlovic S, Roy I, St. Laurent M, Trypaluk C, Unruh D, Yekta M, Bonnin G. 2013. NOAA Atlas 14: precipitation-frequency atlas of the United States. *US Department of Commerce, National Oceanic and Atmospheric Administration, and National Weather Service, Silver Spring, MD*. http://hdsc.nws.noaa.gov/hdsc/pfds/pfds_map_cont.html?bkmrk=co.

Pierson TC. 2005. Hyperconcentrated flow – transitional process between water flow and debris flow. In *Debris-Flow Hazards and Related Phenomena*, Jakob M, Hungr O (eds), Vol. **8**. Springer-Verlag: Berlin Heidelberg; 159–196.

Pierson TC, Costa JE. 1988. A rheologic classification of subaerial sediment-water flows. *Geological Society of America Reviews in Engineering Geology* **7**: 1–12.

Pietraszek JH. 2006. *Controls on post-fire erosion at the hillslope scale*, Colorado Front Range, M.S. thesis. Department of Forest, Rangeland, and Watershed Stewardship. Colorado State University, Fort Collins, CO; 124 pp.

Reid DE, Hickin EJ. 2008. Flow resistance in steep mountain streams. *Earth Surface Processes and Landforms* **33**: 2211–2240.

Rocca ME, Brown PM, MacDonald LH, Carrico CM. 2014. Climate change impacts on fire regimes and key ecosystem services in Rocky Mountain forests. *Forest Ecology and Management* **327**: 290–305.

Schmeer SR. 2014. Post-fire Erosion Response and Recovery, High Park Fire, Colorado, MS thesis. Department of Ecosystem Science and Sustainability. Colorado State University, Fort Collins, CO; 209.

Shakesby RA, Doerr SH. 2006. Wildfire as a hydrological and geomorphological agent. *Earth-Science Reviews* **74**: 269–307.

Smith JA, Baeck ML, Meierdiercks KL, Nelson PA, Miller AJ, Holland EJ. 2005a. Field studies of the storm event hydrologic response in an urbanizing watershed. *Water Resource Research* **41** W10413.

Smith JA, Miller AJ, Baeck ML, Nelson PA, Fisher GT, Meierdiercks KL. 2005b. Extraordinary flood response of a small urban watershed to short-duration convective rainfall. *Journal of Hydrometeorology* **6** (5): 599–617.

Smith MW, Cox NJ, Bracken LJ. 2007. Applying flow resistance equations to overland flows. *Progress in Physical Geography* **31**(4): 363–387.

Tonina D, Jorde K. 2013. Hydraulic modeling approaches for ecohydraulics studies: 3D, 2D, 1D and non-numerical modeling. In *Ecohydraulics: An Integrated Approach*, Maddock I, Harby A, Kemp P, Wood P (eds). Wiley: Chichester, England; 31–74.

Trieste DJ, Jarrett RD. 1987. Roughness coefficients of large floods. In *Proceedings of Irrigation Systems for the 21st Century*. Portland, Oregon, 28–30 July 1987: 32–40.

Wagenbrenner JW, MacDonald LH, Rough D. 2006. Effectiveness of three post-fire rehabilitation treatments in the Colorado Front Range. *Hydrologic Processes* **20**: 2989–3006.

Walling DE. 1977. Assessing the accuracy of suspended sediment rating curves for a small basin. *Water Resources Research* **13**(3): 531–538.

Webb RH, Jarrett RD. 2002. One-dimensional estimation techniques for discharges of paleofloods and historical floods. In *Ancient Floods; Modern Hazards: Principles and Applications of Paleoflood Hydrology; Water Science and Application*, Vol. **5**. American Geophysical Union: Washington, DC; 111–125.

Westerling AL, Hidalgo HG, Cayan DR, Swetnam TW. 2006. Warming and earlier spring increase western US forest wildfire activity. *Science* **313**: 940–943.

Wohl EE. 1998. Uncertainty in flood estimates associated with roughness coefficient. *Journal of Hydraulic Engineering* **124**: 219–223.

Wohl EE. 2013. Migration of channel heads following wildfire in the Colorado Front Range, USA. *Earth Surface Processes and Landforms* **38**: 1049–1053.

Wright DB, Smith JA, Villarini G, Baeck ML. 2013. Long-term high-resolution radar rainfall fields for urban hydrology. *Journal of the American Water Resources Association* **50**(3): 713–734.

Writer JH, Hohner A, Oropeza J, Schmidt A, Cawley KM, Rosario-Ortiz FL. 2014. Water treatment implications after the High Park Wildfire, Colorado. *Journal of American Water Works Association* **106**(4): E189–E199.

Yochum SE. 2015. Colorado Front Range Flood of 2013: peak flows and flood frequencies. *Proceedings of the 5th Federal Interagency Hydrologic Modeling Conference*: Reno, Nevada, 19–23 April 2015.

Yochum SE, Comiti F, Wohl EE, David GCL, Mao L. 2014. Photographic guidance for selecting flow resistance coefficients in high-gradient

channels. USDA Forest Service General Technical Report RMRS-GTR-323: Fort Collins, CO; 91.

Yochum SE, Moore DS. 2013. *Colorado Front Range Flood of 2013: peak flow estimates at selected mountain stream locations*. Fort Collins, CO: USDA Natural Resources Conservation Service; 38.

Zrnić DS, Ryzhkov AV. 1996. Advantages of rain measurements using specific differential phase. *Journal of Atmospheric and Oceanic Technology* **13**: 454–464.

## Supporting Information

Additional Supporting Information may be found online in the supporting information tab for this article.

Figure S1. Plot of cross-section 1 as surveyed in fall 2012, pre-2013 flood, and post-2013 flood. Much of the post-2013 flood topography was disturbed by excavation due to deposition on the neighboring county highway.

Figure S2. Plot of cross-section 2 as surveyed in fall 2012, pre-2013 flood, and post-2013 flood.

Figure S3. Plot of cross-section 3 as surveyed in fall 2012, pre-2013 flood, and post-2013 flood.

Figure S4. Plot of cross-section 4 as surveyed in fall 2012, pre-2013 flood, and post-2013 flood.

Figure S5. Plot of cross-section 5 as surveyed in fall 2012, pre-2013 flood, and post-2013 flood.

Figure S6. Plot of cross-section 6 as surveyed in fall 2012, pre-2013 flood, and post-2013 flood.

Figure S7. Plot of cross-section 7 as surveyed in fall 2012, pre-2013 flood, and post-2013 flood.

Figure S8. Plot of cross-section 8 as surveyed in fall 2012, pre-2013 flood, and post-2013 flood.

Figure S9. Plot of cross-section 9 as surveyed in fall 2012, pre-2013 flood, and post-2013 flood.

Figure S10. Plot of cross-section 10 as surveyed in fall 2012, pre-2013 flood, and post-2013 flood.